Spatially resolved origin of millimeter-wave linear polarization in the nuclear region of 3C 84

Downloaded from: https://research.chalmers.se, 2025-12-04 05:57 UTC

Citation for the original published paper (version of record):
Kim, J., Krichbaum, T., Marscher, A. et al (2019). Spatially resolved origin of millimeter-wave linear polarization in the nuclear region of 3C 84. Astronomy and Astrophysics, 622.
http://dx.doi.org/10.1051/0004-6361/201832920

N.B. When citing this work, cite the original published paper.

research.chalmers.se offers the possibility of retrieving research publications produced at Chalmers University of Technology. It covers all kind of research output: articles, dissertations, conference papers, reports etc. since 2004. research.chalmers.se is administrated and maintained by Chalmers Library

(article starts on next page)

A&A 622, A196 (2019)
https://doi.org/10.1051/0004-6361/201832920
© ESO 2019

Astronomy & Astrophysics

Spatially resolved origin of millimeter-wave linear polarization in the nuclear region of 3C 84⋆

J.-Y. Kim[1], T. P. Krichbaum[1], A. P. Marscher[2], S. G. Jorstad[2,3], I. Agudo[4], C. Thum[5], J. A. Hodgson[6], N. R. MacDonald[1], E. Ros[1], R.-S. Lu[1,7], M. Bremer[8], P. de Vicente[9], M. Lindqvist[10], S. Trippe[11], and J. A. Zensus[1]

[1] Max-Planck Institut für Radioastronomie, Auf dem Hügel 69, 53121 Bonn, Germany
e-mail: jykim@mpifr-bonn.mpg.de
[2] Institute for Astrophysical Research, Boston University, 725 Commonwealth Avenue, Boston, MA 022, USA
[3] Astronomical Institute, St. Petersburg State University, Universitetskij Pr. 28, Petrodvorets, 198504 St. Petersburg, Russia
[4] Instituto de Astrofísica de Andalucía (CSIC), Apartado 3004, 18080 Granada, Spain
[5] Instituto de Radio Astronomía Millimétrica, Avenida Divina Pastora, 7, Local 20, 18012 Granada, Spain
[6] Korea Astronomy and Space Science Institute, 776 Daedeokdae-ro, Yuseong-gu, Daejeon 30455, Korea
[7] Shanghai Astronomical Observatory, Chinese Academy of Sciences, 80 Nandan Road, Shanghai 200030, PR China
[8] Institut de Radio Astronomie Millimétrique, 300 rue de la Piscine, Domaine Universitaire, 38406 Saint-Martin-d'Hères, France
[9] Observatorio de Yebes (IGN), Apartado 148, 19180 Yebes, Spain
[10] Department of Space, Earth and Environment, Chalmers University of Technology, Onsala Space Observatory, 439 92 Onsala, Sweden
[11] Department of Physics and Astronomy, Seoul National University, 1 Gwanak-ro, Gwanak-gu, Seoul 08826, Korea

Received 28 February 2018 / Accepted 16 November 2018

ABSTRACT

We report results from a deep polarization imaging of the nearby radio galaxy 3C 84 (NGC 1275). The source was observed with the Global Millimeter VLBI Array (GMVA) at 86 GHz at an ultrahigh angular resolution of 50 μas (corresponding to ~200R_s). We also add complementary multiwavelength data from the Very Long Baseline Array (VLBA; 15 and 43 GHz) and from the Atacama Large Millimeter/submillimeter Array (ALMA; 97.5, 233.0 and 343.5 GHz). At 86 GHz, we measured a fractional linear polarization of ~2% in the VLBI core region. The polarization morphology suggests that the emission is associated with an underlying limb-brightened jet. The fractional linear polarization is lower at 43 and 15 GHz (~0.3–0.7% and <0.1%, respectively). This suggests an increasing linear polarization degree toward shorter wavelengths on VLBI scales. We also obtain a large rotation measure (RM) of $\sim 10^{5-6}$ rad m^2 in the core at $\gtrsim$43 GHz. Moreover, the VLBA 43 GHz observations show a variable RM in the VLBI core region during a small flare in 2015. Faraday depolarization and Faraday conversion in an inhomogeneous and mildly relativistic plasma could explain the observed linear polarization characteristics and the previously measured frequency dependence of the circular polarization. Our Faraday depolarization modeling suggests that the RM most likely originates from an external screen with a highly uniform RM distribution. To explain the large RM value, the uniform RM distribution and the RM variability, we suggest that the Faraday rotation is caused by a boundary layer in a transversely stratified jet. Based on the RM and the synchrotron spectrum of the core, we provide an estimate for the magnetic field strength and the electron density of the jet plasma.

Key words. galaxies: active – galaxies: jets – galaxies: individual: NGC 1275 – galaxies: individual: 3C 84 – techniques: interferometric – techniques: polarimetric

1. Introduction

Magnetic fields in the vicinity of central black holes (BHs) could play a significant role in the formation, collimation and acceleration of relativistic jets in active galactic nuclei (AGNs; e.g., Blandford & Znajek 1977; Blandford & Payne 1982). Polarization-sensitive very-long-baseline interferometry (VLBI) is an important technique to study the topology and strength of the magnetic fields at the base of AGN jets. Synchrotron theory predicts linear polarization of up to $m_L \sim 70\%$ for optically thin emission and well ordered magnetic fields (Pacholczyk 1970). However, VLBI observations typically find much lower linear polarizations ($m_L \lesssim 5\%$) in the VLBI cores of AGN jets (Lister & Homan 2005; Jorstad et al. 2007). The origin of the weak linear polarization may be due to (i) high synchrotron self-absorption opacity, (ii) a large Faraday depth (e.g., Taylor et al. 2006) and (iii) highly disordered magnetic fields within the observing beam, for example induced by a turbulent plasma (e.g., Marscher 2014). The observed linear polarization can also be reduced by bandwidth depolarization if Faraday rotation is large. Observations at millimeter wavelengths help to overcome the opacity barrier and are less affected by Faraday depolarization than in the centimeter (cm) bands. Furthermore, owing to their small beam size, VLBI observations at millimeter wavelengths (mm-VLBI) have a small in-beam depolarization, in comparison to single-dish or connected interferometer array observations. Thus, mm-VLBI polarimetry is a suitable technique to observe and study the polarization properties of compact radio sources (see also Boccardi et al. 2017).

⋆ The reduced images (FITS format) are only available at the CDS via anonymous ftp to cdsarc.u-strasbg.fr (130.79.128.5) or via http://cdsarc.u-strasbg.fr/viz-bin/qcat?J/A+A/622/A196.

Table 1. Summary of the polarimetric VLBI observations of 3C 84 in May 2015.

Stations	Epoch	ν_{obs}	Beam	I_{peak}	S_{Ptot}	σ_I	PI_{peak}	P_{tot}	σ_P
(1)	(2)	(3)	(4)	(5)	(6)	(7)	(8)	(9)	(10)
	[yy/mm/dd]	[GHz]	[mas, deg]	[Jy bm^{-1}]	[Jy]	[mJy bm^{-1}]	[mJy bm^{-1}]	[mJy]	[mJy bm^{-1}]
VLBA(8)									
+GBT+EB+ON	2015/05/16	86.252	0.048×0.14 (−16.2)	1.82	12.0	0.53	27.7	42.0	5.03
VLBA(10)	2015/05/11	43.115	0.15×0.30 (1.02)	3.82	17.0	1.24	12.3	16.8	1.75
VLBA(10)	2015/05/18	15.352	0.42×0.63 (−8.74)	4.00	28.8	1.30	<2.64	–	0.88

Notes. (1) Antennas participating in each epoch. Numbers in parentheses indicate the number of participating VLBA antennas. (2) The observing epoch in year/month/day format. (3) Center frequency. (4) The restoring beam for the uniform weighting. Minor axis × major axis in mas (the position angle in degrees measured counterclockwise from north). (5) Total intensity peak (in units of Jy per beam). (6) Total flux density integrated over the entire VLBI image. (7) Total intensity rms level. (8) Linear polarization intensity peak (upper limit for 3σ significance). (9) Integrated linearly polarized flux density of the core region obtained by the quadratic sum of the integrated Stokes Q and U flux densities in the region where significant linear polarization intensities are found ("–" means no significant linear polarization in the region displayed in Figs. 2 and 3). (10) The polarization intensity noise level obtained as described in Sect. 2.1.3.

The radio galaxy 3C 84 (Perseus A, NGC 1275) is an intriguing source whose linear polarization in the core region at cm wavelengths is extremely weak (<0.1% at ≤15 GHz; Taylor et al. 2006). This is much lower than typically observed in other AGN jets (Lister & Homan 2005). The source is also relatively nearby, at a redshift of $z = 0.0176$ and a luminosity distance of $d_L = 75$ Mpc (Strauss et al. 1992)[1]. The mass of its central supermassive black hole (SMBH) has been estimated to be $M_{BH} \sim 9 \times 10^8\, M_\odot$ (Scharwächter et al. 2013). The combination of proximity and large black hole mass makes 3C 84 an ideal candidate to study the jet base and its polarization properties with the highest possible angular and spatial resolution, using global mm-VLBI. For the adopted distance an angular scale of 50 μas corresponds to a linear scale of ∼0.0175 pc or ∼203 Schwarzschild radii (R_s).

At 1.3 and 0.9 mm wavelengths (230 and 341 GHz), Plambeck et al. (2014) report a typical degree of linear polarization $m_L \gtrsim 1\%$ using the Combined Array for Research in Millimeter Astronomy (CARMA) and the Submillimeter Array (SMA) with arcsecond scale angular resolution. The authors also find a large rotation measure (RM) of $\sim 9 \times 10^5$ rad m^{-2}. IRAM 30 m Telescope observations at 86 and 230 GHz reveal a typical RM $\sim 7 \times 10^4$ rad m^{-2} (Agudo et al. 2014, 2018b). Both Plambeck et al. (2014) and Agudo et al. (2018b) report polarization variability on monthly timescales at mm wavelengths, implying a small emission region (apparent size $\lesssim 1c \times 1$ month ∼ 0.025 pc ∼ 0.1 mas).

At cm wavelengths and on milliarcsecond scales, however, only low-level polarization is observed. As mentioned above, Very Long Baseline Array (VLBA) observations of the VLBI core of 3C 84 reveal a linear polarization of $m_L \lesssim 0.1\%$ at 15 GHz (upper limit) and $m_L \sim 0.2\%$ at 22 GHz (Taylor et al. 2006). It was suggested that Faraday depolarization with RM $\gtrsim 10^4$ rad m^{-2} could be an explanation (Taylor et al. 2006). The high RM is also consistent with the non-VLBI measurements (Plambeck et al. 2014; Agudo et al. 2018b). However, the limited angular resolution of the previous observations does not yet allow us to precisely localize the polarized emission region nor unambiguously determine the physical origin of the high RM. Observations with the Global Millimeter-VLBI Array (GMVA) help to overcome this limitation. The observing frequency of 86 GHz nicely bridges the gap between the 5 and 22 GHz and 230 GHz observations. This will help to connect the results from the previous studies (e.g., Aller et al. 2003; Agudo et al. 2010, 2018a; Trippe et al. 2012; Plambeck et al. 2014; Nagai et al. 2017), in order to form a self-consistent physical jet polarization model from the cm to the mm regime.

In this paper, we present a new study of the polarization properties of 3C 84 based on GMVA observations at 86 GHz and supplemented by close-in-time VLBA observations at 43 GHz and 15 GHz. In Sect. 2 we describe details of the VLBI observations and the data reduction. Our main findings from the observations are summarized in Sect. 3. The physical implications are discussed in Sect. 4. In Sect. 5 we summarize the results.

2. Observations and data reduction

2.1. GMVA 86 GHz data

The source 3C 84 was observed with the GMVA at 86 GHz in dual circular polarization in May 2015. The source was observed as one of the γ-ray emitting AGN sources, which are monitored by semiannual GMVA observations that complement the VLBA-BU-BLAZAR monitoring program (Jorstad et al. 2017; for the GMVA monitoring see e.g., Rani et al. 2015; Hodgson et al. 2017; Casadio et al. 2017). In this GMVA campaign a total of 11 antennas observed 3C 84: Brewster (BR), Effelsberg (EB), Fort Davis (FD), the Green Bank Telescope (GB), Kitt Peak (KP), Los Alamos (LA), Mauna Kea (MK), North Liberty (NL), Onsala (ON), Owens Valley (OV) and Pie Town (PT). The galaxy was observed in full track mode for 8 h. The data were recorded at an aggregate bitrate of 2 Gbps with two-bit digitization. Using the polyphase filterbank, the data were channelized in eight intermediate frequencies (IFs) per polarization, with an IF bandwidth of 32 MHz, yielding a total recording bandwidth of 2×256 MHz. The data were correlated using the DiFX correlator (Deller et al. 2011) at the Max-Planck-Institut für Radioastronomie (MPIfR) in Bonn, Germany. A summary of details of the observations is given in Table 1.

2.1.1. Total intensity calibration and imaging

The postcorrelation analysis and calibration of the correlated data were done using standard VLBI fringe-fitting and calibration procedures in AIPS (Greisen 1990; see also Martí-Vidal et al. 2012 for the analysis of GMVA data). In the first step of the phase calibration, delay and phase offsets

[1] We assume ΛCDM cosmology with $H_0 = 71$ km s^{-1} Mpc^{-1}, $\Omega_\Lambda = 0.73$ and $\Omega_M = 0.27$.

between the IFs were removed using high signal-to-noise ratio (S/N) fringe detection (so called manual phase calibration). After the phase alignment across the IFs, the global fringe fitting was performed over the full bandwidth, in order to solve for the delays and rates combining all IFs. We set the S/N threshold to five. The number of detections was maximized when we used a relatively long fringe solution interval of four minutes, which was moved forward in time in one-minute steps. In the next step of the process, we performed the a priori amplitude calibration using the AIPS task APCAL, using a priori calibration information provided by each station (system temperatures $T_{\rm sys}$ and elevation dependent gain curves). An opacity correction was performed for stations that did not apply this correction in the delivered system temperature values. Finally, the cross-hand phase and delay offsets of the reference station were determined and removed using AIPS task RLDLY. The UVFITS data were then exported outside AIPS using the AIPS task SPLIT by frequency-averaging the cross power spectra.

At 86 GHz, the atmosphere limits the phase coherence. In order to estimate the effect of coherence losses, we fringe-fitted the data once again using much shorter fringe solution intervals comparable to the coherence time. For this purpose, we set the fringe solution interval to 10 s and adopted the same S/N threshold of five. We also used more narrow fringe search windows for delay and rate (±10 ns and ±25 mHz, respectively). The number of detected scans was reduced dramatically due to the short solution interval. For the detected scans, we found that the short ten-second solution interval did not increase the baseline amplitudes significantly, as long as the phases were not averaged over a longer time interval. (e.g., $\lesssim$10% of decoherence amplitude loss with ten-second time-averaging).

The frequency-averaged (but not yet time-averaged) data were read into the DIFMAP package (Shepherd et al. 1994) for imaging. We flagged outlying visibilities which were caused by known or previously unrecognized antenna problems (such as pointing and focus errors, and bad weather). After an initial phase self-calibration using a point-source model, the visibility data were coherently time averaged over 10 s. We then imaged the source structure in Stokes I by applying the standard, iterative CLEAN and self-calibration steps (for both phase and amplitude). With careful CLEAN and self-calibrations, our CLEAN model was able to reach the maximum correlated flusx density on the shortest uv-spacings (e.g., $\lesssim$200 $M\lambda$). We however note that the limited accuracy of the a-priori calibration for the stations that form the shortest baselines (e.g., PT and LA) could have an effect on the maximum absolute flux density.

In order to correct for a systematic flux density scaling, we combined quasi-simultaneous data from VLBA observations of the source at 15 and 43 GHz (Sect. 2.2) and computed the synchrotron spectrum of the extended jet in the source (at ~2−4 mas from the VLBI core). We then assumed that the observed spectral index of the extended jet components between 15 and 43 GHz is constant (no spectral break) and thus is the same as at the higher frequencies (i.e., between 43 and 86 GHz). Based on this assumption and the observed spectral index of $\alpha_{15-43\,\rm GHz} \sim -0.5$ ($S \propto \nu^{+\alpha}$), we estimated a correction factor for the absolute flux density of the source and further calibrated the data. We also checked the accuracy of the absolute flux density by making use of close-in-time single dish observations and connected interferometer flux measurements of the source between 15 and 343.5 GHz. From this we concluded that the absolute flux density of the source in this epoch could be uncertain by ~30% (see Appendix A for details).

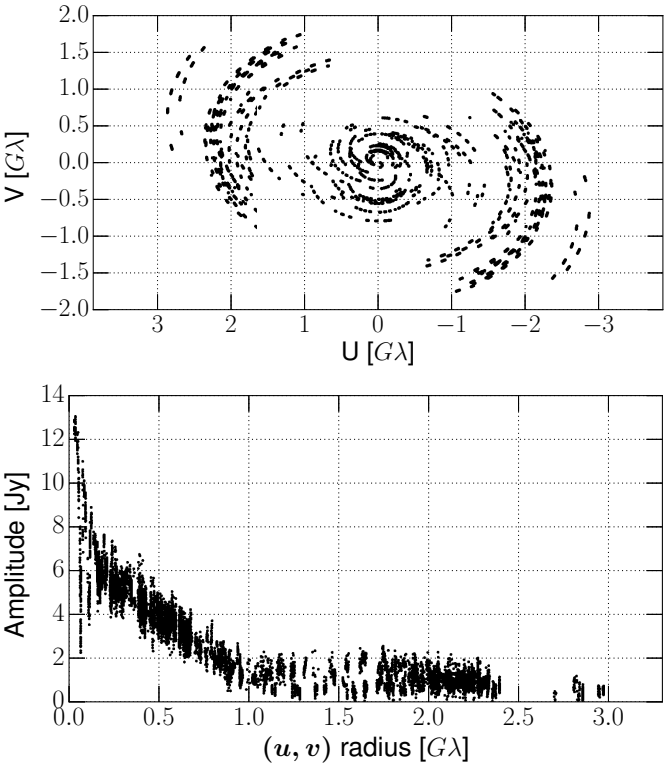

Fig. 1. Stokes I visibilities of the GMVA data. *Top panel*: (u, v)-coverage after the a priori calibration and additional flagging for the imaging. *Bottom panel*: radial distribution of the visibility amplitudes after the last round of CLEAN and self-calibration. The visibility data were binned at 30 s for clarity.

We examined the reliability of the CLEAN model and the self-calibration solutions by comparing the closure phases and amplitudes of the a-priori calibrated data and the CLEAN model. In particular, we compared the differences (and ratios) of the closure phases (and closure amplitudes) between the data and the model. The residual closure phases and the closure amplitude ratios were computed for the histograms of the entire data set. We found that the closure quantities of the a priori calibrated data and the CLEAN model agreed within ~10° for the phases and ~25% for the amplitude, respectively.

A summary of the characteristics of the final 86 GHz Stokes I image is given in Table 1. In Fig. 1 we show the (u, v) coverage of the data set and the visibility amplitudes versus the (u, v)-distances after all the calibrations.

2.1.2. Polarization calibration and imaging

After the total intensity imaging, additional calibration steps were performed in AIPS in order to remove residual gain offsets between the RCP and LCP receivers and the polarization leakage effects. In particular, the antenna instrumental polarization solutions (D-terms) were determined using the AIPS task LPCAL (Leppanen et al. 1995). We derived the D-terms from other more compact calibrator sources including 3C 454.3, BL Lac, CTA 102 and OJ 287, which were observed in the same session. We also derived the D-terms from 3C 84 itself, which is facilitated by (i) its core-dominace at millimeter wavelengths (see Sect. 3) and (ii) wide parallactic angle coverage in this data set. We show two linear polarization images of 3C 84 in Appendix B for D-term solutions derived from CTA 102 and OJ 287. The

Table 2. Summary of the antenna D-terms at 86 GHz.

Station	RCP		LCP	
	m [%]	χ [deg]	m [%]	χ [deg]
(1)	(2)	(3)	(4)	(5)
BR	5.8 ± 2.7	−(106 ± 16)	7.2 ± 2.7	−(48 ± 20)
EB	4.5 ± 2.1	56 ± 24	2.3 ± 2.5[a]	98 ± 40[a]
FD	7.9 ± 2.9	23 ± 13	7.0 ± 3.6	−(141 ± 25)
GB	1.7 ± 2.4[a]	−(162 ± 46)[a]	2.6 ± 1.3	−(66 ± 44)[a]
KP	3.1 ± 2.8	178 ± 30	3.8 ± 1.7	88 ± 14
LA	10.7 ± 1.6	139 ± 9	10.1 ± 2.1	32 ± 13
MK	3.9 ± 3.1	11 ± 25	4.3 ± 1.9	−(90 ± 23)
NL	4.8 ± 1.6	−(167 ± 21)	3.7 ± 1.3	70 ± 13
ON	5.9 ± 1.9	−(178 ± 27)	4.8 ± 2.4	−(4 ± 36)
OV	3.6 ± 2.4	−(48 ± 38)	5.4 ± 1.7	−(127 ± 21)
PT	8.2 ± 5.6	7 ± 8	9.6 ± 3.4	−(134 ± 21)

Notes. The Green Bank Telescope was used as the reference antenna. The columns show (1) the station code, (2,3) the amplitude (m) and phase (χ) of the D-terms for the RCP and (4,5) the same for the LCP. [(a)]Small D-term amplitudes induce large uncertainties in the D-term phases.

maps show a broadly consistent appearance of the polarization. In order to obtain a final set of D-terms, we vector-averaged the D-terms and created the final polarization image of 3C 84 for further analysis. Confidence in the final D-terms was obtained by imaging the polarized structure of the calibrators. Their GMVA polarization images showed good agreement with contemporaneous VLBA 43 GHz polarization images available from the VLBA-BU-BLAZAR database[2], but with more fine-scale structure seen in the GMVA images. Those images will be published later elsewhere.

The final D-term solutions are shown in Table 2. Their errors are estimated based on the standard deviation of the different D-term values for each station and polarization.

The absolute electric vector position angle (EVPA) of 3C 84 was calibrated using OJ 287, 3C 454.3 and BL Lac. These calibrators were also observed as part of the POLAMI (Polarimetric Monitoring of AGNs at Millimeter Wavelengths) program[3] (Agudo et al. 2018a) by the IRAM 30 m Telescope, which was equipped with the XPOL polarimeter (Thum et al. 2008). We estimated the overall uncertainty of the EVPA measurements in GMVA data using the following procedure: first, the measurement error of the 86 GHz EVPA in the IRAM 30 m Telescope data is ∼2−7 deg for different sources and for this particular epoch (see also Agudo et al. 2018a). By deriving the VLBI EVPA correction values from multiple calibrators, we adopted a conservative absolute EVPA uncertainty of ∼10 deg. Second, the polarization angle of the source and the D-term phases are correlated and uncertainties of the latter could affect the accuracy of the former (see, e.g., Eqs. (3) and (13) of Leppanen et al. 1995). The average phase errors of the D-terms was ∼24 deg (Table 2). Accordingly, we estimated that the corresponding EVPA uncertainty would be ∼24/2 = 12 deg. Third, we computed the peak-to-noise of the polarization features in Stokes Q and U and propagated the errors to estimate the EVPA uncertainty due to the thermal noise. Under the assumption that these three measurement errors are uncorrelated, we can add them in quadrature. For a S/N of ∼5, this led to an overall EVPA uncertainty of ∼17 deg in this GMVA observation.

2.1.3. Estimating noise levels in the polarization image

The Rice bias correction for polarization measurements (see, e.g., Wardle & Kronberg 1974; Montier et al. 2015a,b) requires an accurate estimation of the S/N. We simulated the probability density distribution of the noise in the linear polarization intensity image, $\sigma_{\rm P}$, by performing a Monte-Carlo simulation. First, we computed the 1σ noise levels for Stokes Q and U by fitting Gaussian functions to pixel value histograms of source-free regions in the Stokes Q and U images. We then simulated Gaussian-distributed noises for Q and U and added them in quadrature to obtain the probability distribution of the polarization noise. By calculating the 68%, 97% and the 99.7% confidence levels, we obtained the noise values of 5.7, 9.5 and 14.0 mJy beam^{-1} for the conventional 1σ, 2σ, and 3σ levels, respectively. Based on this, we adopted $1\sigma_{\rm P} \sim 5$ mJy beam^{-1} at 86 GHz.

We note that this value is higher than the noise in the Stokes I image ($\sigma_{\rm I} \sim 0.5$ mJy beam^{-1}). In the ideal case, the noise level of a linear polarization map, $\sigma_{\rm P}$, is expected to be comparable to or lower than that of the total intensity map, $\sigma_{\rm I}$, because the latter is often dynamic-range limited (see, e.g., Thompson et al. 2017). However, this is not the case if systematic polarization calibration errors dominate the polarization noise (e.g., due to errors in the D-terms). Thus, we checked if the increased noise level in the linear polarization map could be due to uncertain D-term solutions. Following Roberts et al. (1994; see also Hovatta et al. 2012), we estimated the error from D-term calibration as follows:

$$\sigma_{\rm Dterm} = \frac{\Delta m}{\sqrt{N_{\rm ant} \times N_{\rm IF} \times N_{\rm scan}}} \sqrt{I^2 + (0.3 \times I_{\rm peak})^2}, \quad (1)$$

where Δm is the error of the D-term amplitudes, $N_{\rm ant}$ is the number of the antennas, $N_{\rm IF}$ is the number of IFs, $N_{\rm scan}$ is the total number of independent scans with different parallactic angles, I is the total intensity pixel values and $I_{\rm peak}$ is the peak value of the total intensity image. As shown in Table 2, the D-term amplitudes are uncertain by ∼2−4% (the largest uncertainty of ∼5% is found for RCP at PT). Therefore, we assumed a characteristic value of $\Delta m \approx 0.03$. For the GMVA data of 3C 84, we adopt $N_{\rm ant} = 11$ and $N_{\rm IF} = 8$. The number of independent scans including all the antennas was $N_{\rm scan} = 8$. This gave us a characteristic $\sigma_{\rm Dterm} \sim 10^{-3} \times I_{\rm peak}$. For $I_{\rm peak} = 1.8$ Jy beam^{-1}, we obtain $\sigma_{\rm Dterm} \sim 2$ mJy beam^{-1}. The order of $\sigma_{\rm Dterm}$ appears to be in agreement with our estimation of $\sigma_{\rm P}$, suggesting that residual polarization leakages may dominate the polarization noise in our 86 GHz image.

2.2. Contemporaneous 43- and 15 GHz VLBA data

On short timescales of approximately one week or less, the structural variability of 3C 84 is likely negligible because of the known slow apparent jet speed of $0.1c \sim 0.1$ mas yr $= 2\,\mu$as week^{-1} in the core region of 3C 84 (Walker et al. 1994; Suzuki et al. 2012). This allows us to combine the 86 GHz data with quasi-contemporaneous observations at other frequencies.

We made use of archival polarimetric VLBA data of 3C 84 provided by the MOJAVE program[4] (15 GHz; Lister & Homan 2005) and the VLBA-BU-BLAZAR monitoring program

[2] https://www.bu.edu/blazars/VLBAproject.html
[3] http://polami.iaa.es/
[4] https://www.physics.purdue.edu/MOJAVE/

(43 GHz; Jorstad et al. 2017). We have chosen a set of 15- and 43 GHz data which were obtained closest in time to the GMVA observations. The archival data were gathered with the same dual polarization setup (RCP and LCP) and the same total bandwidth of 2×256 MHz. The Stokes I, Q and U maps again were obtained using DIFMAP, averaging the visibilities over the whole observing bandwidth. At these two frequencies, we estimated the polarization image noise levels $\sigma_{\rm P}$ in the same way as described in Sect. 2.1.3. The $\sigma_{\rm P}$ values were comparable to $\sigma_{\rm I}$, indicating that at these lower frequencies the systematic uncertainties in the linear polarization due to errors in the D-terms were small. A summary of the two data sets is given in Table 1.

For the absolute EVPA measurement error (i.e., those arising from the D-term calibration and absolute EVPA correction), we adopted 5 deg and 10 deg at 15 and 43 GHz based on Lister & Homan (2005) and Jorstad et al. (2005), respectively. The overall uncertainty for the EVPA was then estimated in the same way as we described in Sect. 2.1.2 by adding the systematic and thermal errors in quadrature.

In addition, the VLBA-BU-BLAZAR program provides the VLBA 43 GHz data at four different frequencies in the 43 GHz band (43.0075, 43.0875, 43.1515 and 43.2155 GHz). Their polarization calibration was performed separately for each IF with respect to the D-terms and EVPA values (see Sect. 3.1 of Jorstad et al. 2005). Therefore, we created additional 43 GHz polarization images of the source for each of the four IFs separately, in order to resolve the $n\pi$ angle ambiguity in the rotation measure analysis and to check for a possible large EVPA rotation inside the 43 GHz band.

2.3. Noncontemporaneous VLBA data at 43 GHz

We also analyzed other VLBA 43 GHz data of 3C 84 available from the BU database in order to study the time variability of the total flux and the linear polarization over a longer period. We specifically focused on observations performed in 2015 (eight epochs; Feb., Apr., May, Jun., Jul., Aug., Sep. and Dec.). We imaged the source again by applying some additional data flagging when systematically large errors were clearly seen in some antennas or scans. The full-polarization images available from the BU database reveal a weak polarization feature in the core region of 3C 84 in all eight epochs in 2015. In our imaging, we recovered a very similar polarization morphology in most epochs, however some epochs (Feb., Jun., Aug. and Dec.) appeared to be more limited in polarization fidelity, possibly due to the limited number of scans or other systematic errors. Therefore, we did not include these polarization images in our analysis. Overall, repeatedly appearing and therefore reliable polarization features have been detected in four (Apr., May, Jul. and Sep.) out of the eight epochs. We also measured the unpolarized core flux for all eight epochs using the MODELFIT routine implemented in DIFMAP and analyzed their uncertainties following Schinzel et al. (2012; see Sect. 2.5). We summarize details for these data in Appendix C.

2.4. Contemporaneous ALMA data

Finally, we made use of contemporaneous (May 2015) linear polarization measurements of 3C 84 from the Atacama Large Millimeter/submillimeter Array (ALMA) Calibrator Source Catalogue[5]. The source was observed at 97.5, 233.0 and 343.5 GHz and was not resolved up to the baseline length of 537.5 $k\lambda$ at all frequencies. Therefore, we constrained the source size to be $<1/(537.5\times10^3)$ rad $\approx$ 0.38 arcsecs. Table 3 summarizes the archival ALMA polarization measurements.

[5] https://almascience.eso.org/alma-data/calibrator-catalogue

Table 3. Summary of the ALMA archival data.

Epoch	$\nu_{\rm obs}$	$S_{\rm tot}$	$m_{\rm L}$	EVPA
(1)	(2)	(3)	(4)	(5)
[yyyy/mm/dd]	[GHz]	[Jy]	[%]	[deg]
2015/05/31	97.5	17.14 ± 0.57	0.6 ± 0.3	82.1 ± 19.7
	233.0	9.82 ± 0.33	1.0 ± 0.3	−(29.1 ± 12.1)
	343.5	6.85 ± 0.23	0.3 ± 0.3	18.3 ± 42.9

Notes. The columns show (1) the observing epoch, (2) the central frequency, (3) the total flux, (4) the degree of the linear polarization and (5) the EVPA.

2.5. Modelfitting, polarization measurements and their uncertainties

In order to parameterize the size and the flux density of the VLBI core region in Stokes I, we made use of the MODELFIT procedure implemented in DIFMAP. We fitted circular Gaussians to the visibilities at each frequency and estimated their uncertainties following Schinzel et al. (2012). For the absolute flux density at 86 GHz, we conservatively adopted an uncertainty of ∼30% based on the limitation of the absolute flux calibration in this epoch.

The polarization components were identified by the local maxima of their linearly polarized intensities in the image plane (see Figs. 3 and 7). For each component, we defined a circular aperture whose diameter matched the mean beam size and was centered at the local peak of the polarized intensity. The properties of the polarized components – meaning the Stokes I flux density S, the linearly polarized flux density P, the degree of linear polarization $m_{\rm L}$ and the EVPA χ – were then determined from the spatially integrated Stokes I, Q, and U flux densities. Specifically, the integrated flux densities and the polarization parameters were computed using the following equations.

$$Q_{\rm tot} = \Sigma Q_{i,j} \times A_{\rm pixel}/A_{\rm Beam} \quad \text{(in Jy)}, \tag{2}$$
$$U_{\rm tot} = \Sigma U_{i,j} \times A_{\rm pixel}/A_{\rm Beam} \quad \text{(in Jy)}, \tag{3}$$
$$S = \Sigma I_{i,j} \times A_{\rm pixel}/A_{\rm Beam} \quad \text{(in Jy)}, \tag{4}$$
$$P = \sqrt{Q_{\rm tot}^2 + U_{\rm tot}^2} \quad \text{(in Jy)}, \tag{5}$$
$$m_{\rm L} = 100 \times P/S \quad \text{(in percent)}, \tag{6}$$
$$\chi = 0.5 \arctan(U_{\rm tot}/Q_{\rm tot}) \quad \text{(in radian)}, \tag{7}$$

where $I_{i,j}$, $Q_{i,j}$ and $U_{i,j}$ are the corresponding Stokes intensity values at each pixel (i, j) in Jy beam^{-1} and $A_{\rm pixel}$ and $A_{\rm Beam}$ are the pixel and the beam area in square mas, respectively[6]. In these calculations, we also corrected for the Rice bias in the polarization intensity value at each pixel by following Wardle & Kronberg (1974). We assumed that the uncertainty of P was 30% at all frequencies. For S, we assumed 10% uncertainties at ≤43 GHz (e.g., Lister & Homan 2005; Jorstad et al. 2005)

[6] We computed the area under the elliptical Gaussian beam, $A_{\rm Beam}$, by $A_{\rm Beam} = \pi\psi_{\rm maj}\psi_{\rm min}/4\ln 2$ where $\psi_{\rm maj,min}$ are the FWHM of the elliptical Gaussian along the major and the major axis, respectively. The areas of individual pixels, $A_{\rm pixel}$, are 0.01×0.01, 0.02×0.02 and 0.03×0.03 square mas at 86, 43 and 15 GHz, respectively.

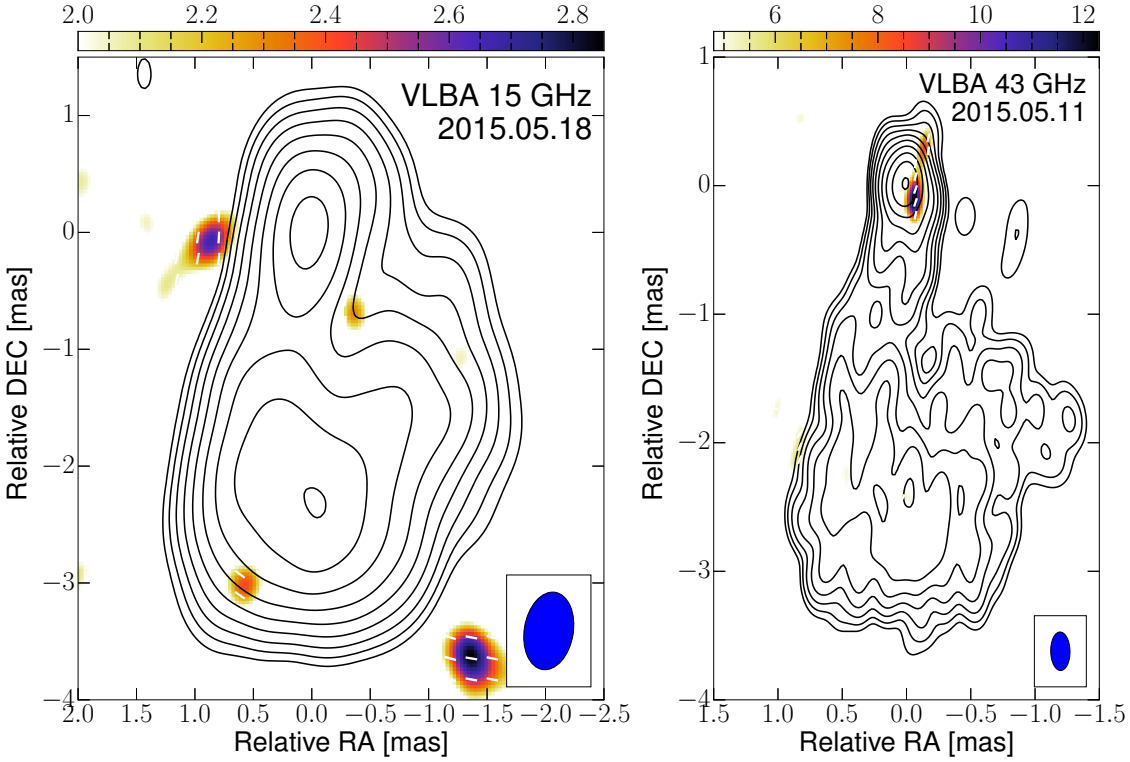

Fig. 2. Polarimetric VLBI images of 3C 84 at 15 and 43 GHz. In both panels, the contours show the total intensity and increase by a factor of two from the lowest level. The color scale represents the polarized intensity (in mJy beam^{-1}). The white bars in the images display the apparent EVPA. The blue ellipse in the bottom right corner shows the restoring beam. *Left panel*: VLBA 15 GHz image. The contours start at 30 mJy beam^{-1}. The color scale starts at 2.0 mJy beam^{-1}. *Right panel*: VLBA 43 GHz image. The contours start at 7 mJy beam^{-1}. The color scale starts at 4.8 mJy beam^{-1}.

but 30% at 86 GHz as explained before. The uncertainty of $m_{\rm L}$ was then obtained by propagating the errors of the integrated flux densities. The EVPA error was calculated as described in Sect. 2.1.2.

3. Results

3.1. Total intensity structure and the core flux

In Fig. 2 we show the quasi-simultaneous polarimetric VLBI images of 3C 84 at 15 and 43 GHz in May 2015. The GMVA 86 GHz images are shown in Fig. 3 with two different restoring beams in order to better illustrate both the extended and inner jet structure. The source clearly shows a limb-brightened jet at high frequencies (≥43 GHz). The limb-brightening is visible up to ∼2 mas from the core. We made transverse cuts to the jet at a core separation $z \sim 0.4$ mas at 43 and 86 GHz using the full-resolution image (Fig. 3, right) and show the intensity profiles of the slices in Fig. 4. The limb-brightened transverse structure is consistent with previous deep single-epoch (Nagai et al. 2014) and long-term (Jorstad et al. 2017) VLBA 43 GHz observations of the source. At 86 GHz, the improved angular resolution resolves the edge-brightened structure down to ∼0.2 mas core distance. Remarkably, within the inner 0.2 mas from the intensity peak, the nuclear region appears substantially resolved in the E–W direction and shows a complex morphology. The 86 GHz core is well represented by a single circular Gaussian component whose FWHM size is comparable to the 43 GHz core. However, the visibilities at long baselines (∼1.0–2.5$G\lambda$) suggest the presence of a more complex subnuclear structure (see Fig. 1). On larger scales, the overall source structure is quite similar to that shown in the 43 GHz image (cf. Figs. 2 and 3), but the extended jet emission at larger core separations is overall fainter. A more detailed study of the total intensity structure is beyond the focus of this paper and will be presented elsewhere.

In Table 4 we show the flux densities $S_{\rm mod}$ and FWHM sizes of the core at 15, 43 and 86 GHz obtained with the MODELFIT procedure of DIFMAP. We fitted a single power-law to the core spectrum, that is $S \propto \nu^{+\alpha}$ where ν is the observing frequency and α is the spectral index. The results are shown in the left panel of Fig. 5. We find that the spectrum of the VLBI core is slightly inverted up to 86 GHz with a spectral index of $\alpha = 0.51 \pm 0.10$. We also show the time variation of the core flux at 43 GHz in Fig. 6. In the same figure we also provide the peak values obtained with a circular Gaussian beam of 0.3 mas. The core brightens by ∼2 Jy during 2015 and reaches a local maximum during June and July 2015.

3.2. Linear polarization in the core region

In Fig. 7 we show the linear polarization structure in the core region at 43 and 86 GHz in more detail, restoring the maps with the VLBA 43 GHz beam at both frequencies for better comparison. In May 2015, we detect linear polarization features in the core at high significance ($PI_{\rm peak}/\sigma_{\rm P} \sim 7.0$ and 5.5 at 43 and 86 GHz, respectively; see Table 1). At 15 GHz, no significant polarization features appear in the nuclear region. The polarization features at both 43 and 86 GHz are slightly offset from the peak of the total intensity. The features P1 and P2 (i.e., P2a+P2b) are separated by ∼0.2 mas in the E–W orientation, and could possibly be associated with the edges of the underlying limb-brightened jet seen at 22 GHz by recent RadioAstron

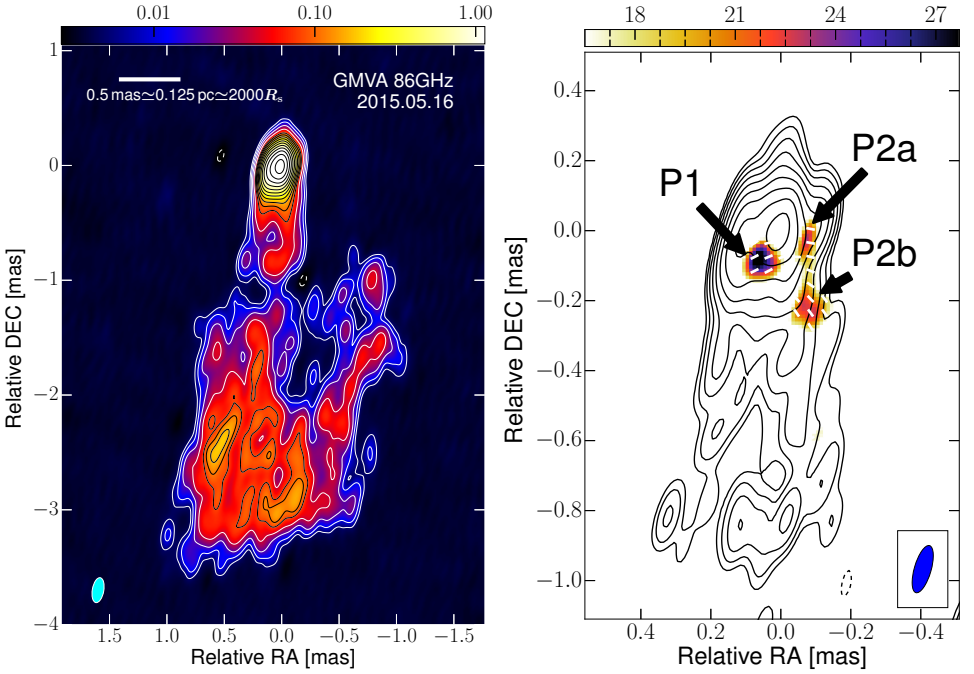

Fig. 3. GMVA 86 GHz images of 3C 84. In both panels, the contours show the total intensity and increase by a factor of two from the lowest level (5 mJy beam^{-1}). A negative contour of −5 mJy beam^{-1} is also shown with dashed lines. *Left panel*: stokes *I* image restored with an elliptical beam of 0.22×0.10 mas and position angle of −10°. This beam is larger than the full resolution attainable with the GMVA. The peak of this image is 3.04 Jy beam^{-1}. The cyan ellipse in the bottom-left corner illustrates the elliptical beam. The color scale represents the Stokes *I* pixel values in Jy beam^{-1}. The white bar and the text in the upper left corner denote the projected spatial scale of the image. *Right panel*: inner jet structure obtained with the full angular resolution of the GMVA. The color scale represents the linear polarization intensity and starts from 16.5 mJy beam^{-1}.

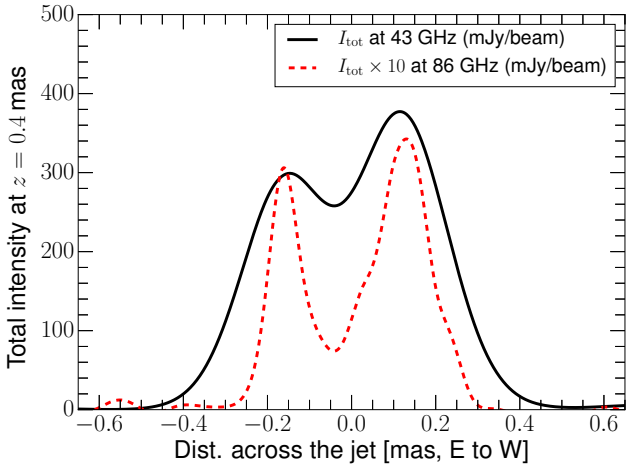

Fig. 4. Transverse jet intensity profiles at 43 GHz (black solid line) and 86 GHz (red broken line) obtained at 0.4 mas core distance as a function of distance across the jet (increasing toward west).

observations (e.g., Giovannini et al. 2018). The P2 component is present in both maps at similar locations. However, the P1 component in the 86 GHz image has no clear counterpart at 43 GHz. Using the pixel values at the position of P1, we estimate its $3\sigma_P$ upper limit to m_L to be $\lesssim$0.2% at 43 GHz. At 43 GHz, there exists another polarized feature (∼8 mJy beam^{-1}) at a separation of ∼0.3 mas to the north of the core, perhaps associated with a counterjet. We searched the VLBA-BU-BLAZAR database for evidence in support of significant polarization north of the main intensity peak in several epochs. While the polarization detection close to the total intensity peak can be seen in many epochs, we found polarization north of it only in a few epochs. Therefore we do not find strong evidence for a persistent polarization on the counterjet side. Except for this faint northern polarization feature, the 43 GHz VLBA polarization images in the other epochs show similar linear polarization flux densities in the core region, although the relative position of the polarization peak seems to change with time (see Appendix C).

Table 4. VLBI core properties in May 2015.

ν_{obs} (1) [GHz]	S_{mod} (2) [Jy]	$FWHM$ (3) [mas]
86	5.6 ± 1.7	0.13 ± 0.04
43	4.8 ± 0.7	0.14 ± 0.01
15	2.6 ± 0.4	0.27 ± 0.02

Notes. The columns show (1) the central observing frequency and (2),(3) the total flux and the FWHM size of the VLBI component obtained by the Gaussian model fitting.

At 86 GHz, the degrees of the linear polarization m_L of the polarized components are in the range of ∼3−6% when convolved with the small GMVA observing beam. The 86 GHz m_L values decrease to ∼1−2% when convolved with the VLBA 43 GHz beam. For the P2 component, the m_L value is significantly lower at 43 GHz (∼0.4−0.5% in this epoch). At 15 GHz, the nondetection suggests a 3σ upper limit to m_L of $\lesssim$0.1%, which is in agreement with the results of Taylor et al. (2006). In order to minimize the effect of the different angular resolutions of the VLBA and the GMVA images, we now determine the polarization properties convolving the maps with the same VLBA 43 GHz beam (Fig. 7) and compare the results in the following analysis. Table 5 provides a summary of the properties of the polarized components in May 2015 (see Appendix C for results at 43 GHz at other epochs).

In order to investigate the frequency dependence of the linear polarization of the core region, we combined linear polarization measurements from the literature with the data from this paper. The results are shown in the right panel of Fig. 5. The linear polarization of the core clearly shows an increasing trend with frequency, which can be represented by a power-law fit $m_L \propto \nu^{0.77\pm0.18}$, in which we have combined all available m_L measurements. We note that the index of the power law could be affected by some systematic uncertainties due to the different angular resolutions of the telescopes. Nevertheless, we

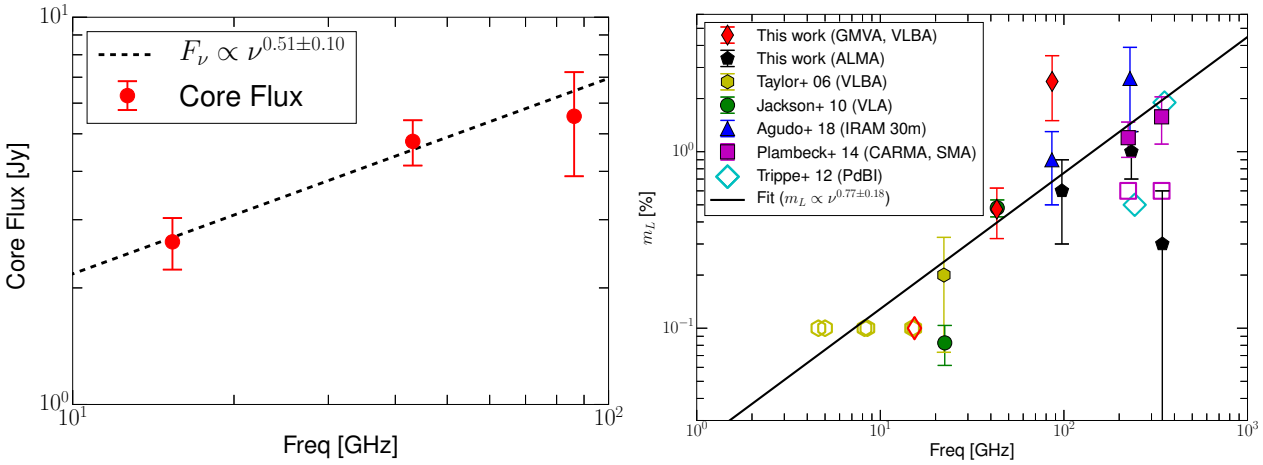

Fig. 5. *Left panel*: total intensity spectrum of the VLBI core region between 15 and 86 GHz. *Right panel*: degree of linear polarization in the VLBI core region obtained from this work and previous VLBA observations (Taylor et al. 2006) and integrated values from the literature (Jackson et al. 2010; Trippe et al. 2012; Plambeck et al. 2014; Agudo et al. 2018b). All the VLBI polarization measurements were made from the pixel values near the peak of the Stokes *I*. Filled and open symbols of the same marker indicate measured values and upper limits, respectively. Citations and corresponding instruments are shown in the legend. We note that at 230 GHz only upper limits were observed before May 2011 (Trippe et al. 2012; Plambeck et al. 2014). After October 2011, Plambeck et al. (2014) report a significantly higher linear polarization degree.

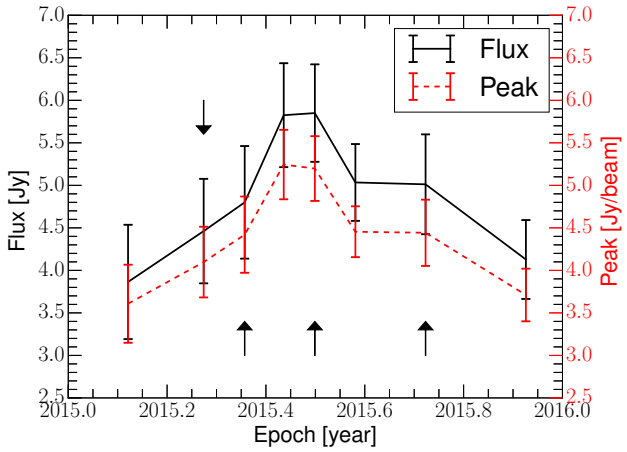

Fig. 6. VLBA 43 GHz core flux and the peak values during 2015. Arrows indicate epochs during which reliable polarization has been detected.

can clearly see that both VLBI and non-VLBI measurements show an increase of linear polarization degree toward higher frequencies.

3.3. Rotation measure between 43 and 344 GHz in May 2015

We determine the RM associated with the Faraday rotation by measuring the variation of the observed EVPA with frequency. When a linearly polarized wave at a wavelength λ passes through magnetized plasma, the intrinsic EVPA of the emission $\chi_{\rm int}$ is rotated and the observed EVPA $\chi(\lambda)$ is

$$\chi(\lambda) = \chi_{\rm int} + {\rm RM} \times \lambda^2. \quad (8)$$

The RM is determined by the gradient of $\chi(\lambda)$ versus λ^2 after solving for the $n\pi$ ambiguity in the angle. To resolve the $n\pi$ ambiguity, we assume that most of the polarized flux observed by the ALMA at 97.5, 233.0 and 343.5 GHz originates from the same VLBI core region. This assumption appears to be reasonable based on the flat spectrum of the linearly polarized flux density between 97.5 and 233.0 GHz measured by ALMA (~100 mJy at both frequencies; see Table 3). We then compute the integrated Stokes Q and U flux densities of the VLBI core region at 43 and 86 GHz to obtain the spatially integrated EVPAs. The spatially integrated EVPAs within the 43 GHz band are shown in Table 5. At 86 GHz, the integrated EVPA is $\chi = -(70 \pm 16)$ deg. Subsequently, we compare all these EVPAs simultaneously to find a best λ^2 fit.

We resolve the $n\pi$ ambiguity by following Hovatta et al. (2012). The authors determined the smallest possible EVPA rotations at each frequency to achieve a statistically acceptable fit with the λ^2 model. Similarly, we rotated the 86.0, 97.5, 233.0, and 343.5 GHz EVPAs by $(n_1, n_2, n_3, n_4)\times\pi$, respectively, where $n_i \in (-30, -29, \ldots, 29, 30)$ and $i \in (1, 2, 3, 4)$. We then calculated corresponding χ^2 values for each rotation. We note that $n = 30$ corresponds to RM $\sim 10^8$ rad m^{-2} for the frequency range considered here. The RM of $\sim 10^8$ rad m^{-2} is also equivalent to a single 180° wrap within the 43 GHz band. Therefore, we are assuming that there is no RM $\gtrsim 10^8$ rad m^{-2} in the source (cf. Plambeck et al. 2014). For the same reason, we did not apply the $n\pi$ rotation within the 43 GHz band. We then chose a set of n_i which provided the minimum χ^2 value.

We find a best λ^2 fit with $n_1 = -2$, $n_2 = -3$, $n_3 = -3$ and $n_4 = -3$ (corresponding $\chi^2 = 3.52$ and the reduced $\chi^2 = 0.59$; see Fig. 8). Accordingly, we obtain RM $= (2.02\pm0.03)\times10^5$ rad m^{-2} and $\chi_{\rm int} = -(578 \pm 7)$ deg (or equivalently $\chi_{\rm int} = -(38 \pm 7)$ deg). We note this RM is comparable to RM $\sim 9 \times 10^5$ rad m^{-2} previously reported by Plambeck et al. (2014).

3.4. Rotation measure within the 43 GHz band

We applied the same RM fitting procedure to the multiepoch VLBA 43 GHz data using the EVPAs measured at the four different IFs. We tested the significance of the EVPA rotation within the 43 GHz band for 3C 84 by performing the same analysis to the core regions of two comparison sources 0235+164 and 3C 279, which were observed in the same epochs by the VLBA-BU-BLAZAR monitoring program. The instrumental polarization calibration and the sub-band EVPA calibration for the two sources were completely identical to those of 3C 84 during 2015. Therefore, we expect that the EVPA change within

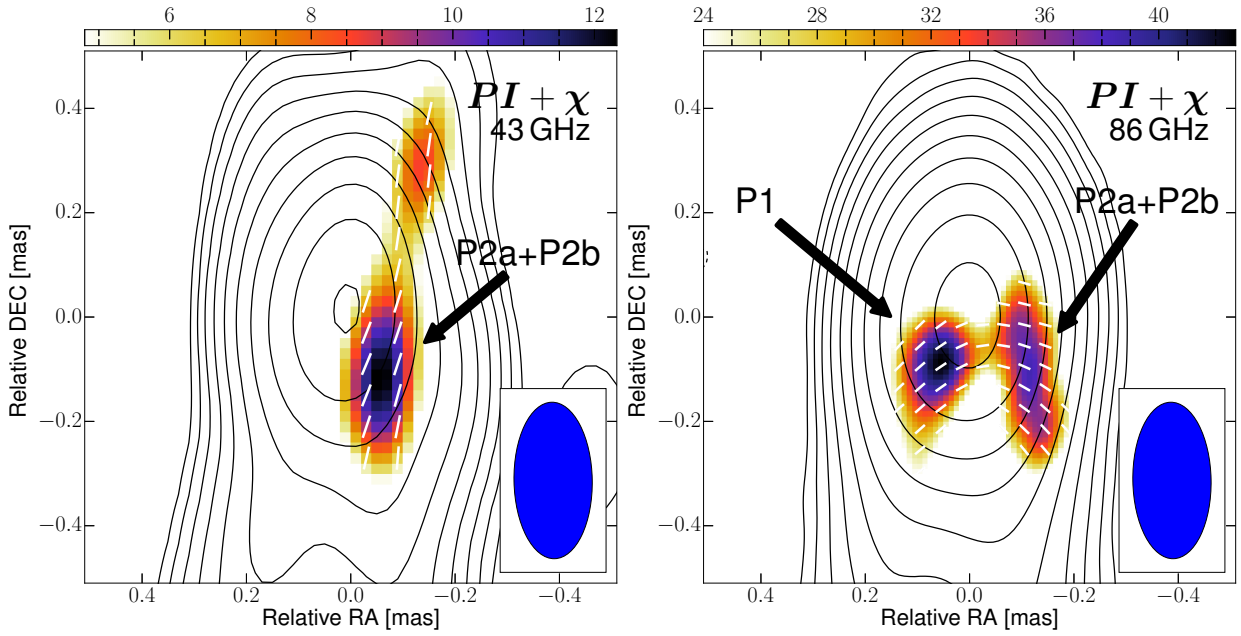

Fig. 7. Comparison of the total intensity, the polarized intensity (PI) and the polarization angle (χ) in the nuclear region at 43 and 86 GHz. The maps are restored with the same VLBA 43 GHz CLEAN beam and displayed over the same RA and Dec ranges (±0.5 mas). The arrows show the polarized component identifications. *Panel a*: as in the central panel of Fig. 2 (43 GHz) but zoomed into the core. *Panel b*: GMVA 86 GHz total and linear polarization image restored with the VLBA 43 GHz beam. The contours start at 6 mJy beam^{-1} and increase by a factor of two from the lowest level. The color scale starts from 24 mJy beam^{-1}.

Table 5. Properties of the polarized components in May 2015.

$\nu_{\rm obs}$ (1) [GHz]	ID (2)	S_ν (3) [Jy]	m_ν (4) [%]	χ_ν (5) [deg]
86.252	P1	0.70 ± 0.21	3.4 ± 1.4	−(54 ± 17)
	P1[a]	1.5 ± 0.4	1.4 ± 0.6	−(43 ± 17)
	P2a	0.27 ± 0.08	6.3 ± 2.7	−(89 ± 17)
	P2b	0.05 ± 0.02	44 ± 20[b]	47 ± 17[b]
	P2a+P2b[a]	1.3 ± 0.4	2.2 ± 0.9	71 ± 17
43.0075	P2a+P2b	2.0 ± 0.2	0.44 ± 0.14	−(9 ± 10)
43.0875			0.49 ± 0.16	−(20 ± 10)
43.1515			0.53 ± 0.17	−(24 ± 10)
43.2155			0.43 ± 0.13	−(15 ± 10)
15.352		N/A	<0.1[c]	N/A

Notes. The columns show (1) the central frequency, (2) the component identification, (3) the Stokes I flux density, (4) the degree of linear polarization and (5) the EVPA. The Stokes I flux densities are consistent at the four separate frequencies within the 43 GHz band and we omit the numbers for the other three 43 GHz sub-bands. [(a)]Obtained from the image in panel (B) of Fig. 7. [(b)]The component is associated with the outer edge of the jet and could have higher systematic uncertainties than our estimation. [(c)]3σ upper limit from the nondetection.

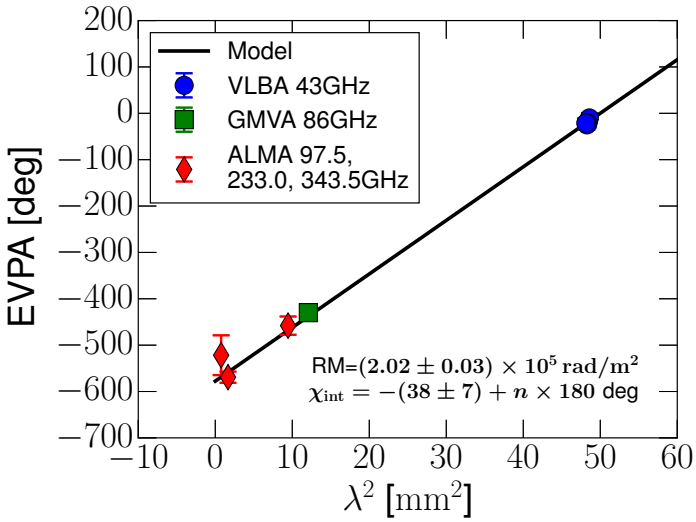

Fig. 8. Spatially integrated EVPA vs. the squared wavelength λ^2 (error bars) and the best λ^2 fit (solid line) in May 2015.

the 43 GHz band will be systematically the same for the three sources if the EVPA changes are dominated by residual calibration errors.

In Fig. 9 we show the EVPAs χ for 0235+164 and 3C 279, with respect to their mean values, $\langle\chi\rangle$. Within the 43 GHz band, the EVPA of 3C 279 varies only by ≤6 deg in all epochs (≤8 deg for 0235+164). This is insignificant compared to our presumed ten-degree angle uncertainty at 43 GHz. In addition, the two sources show strongly correlated EVPA offset from their mean values in all epochs. From this we determine that the 43 GHz in-band RM values smaller than ∼(2−3) × 10^5 rad m^{-2} are insignificant against the residual calibration errors.

After this consideration, we show the EVPAs measured from the core of 3C 84 at the 43 GHz band in Fig. 10. The corresponding RM values obtained from the fitting are shown in Table 6 and a plot of the RM versus time is given in Fig. 11. In contrast to 0235+164 and 3C 279, 3C 84 shows much larger EVPA variation within the 43 GHz band (15−21 deg). This EVPA variation with wavelength is larger than the residual calibration errors that we estimated. This results in a significant RM

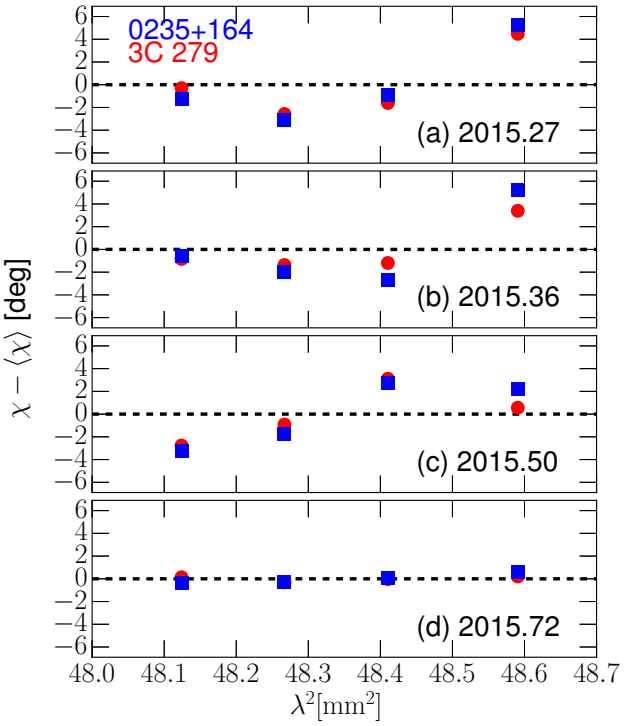

Fig. 9. Variation of the EVPA in each sub-band, χ, with respect to the mean EVPA, $\langle\chi\rangle$. Blue squares and red circles are for 0235+164 and 3C 279, respectively. Error bars are omitted for clarity. We note the strong correlation between the two sources.

($|\mathrm{RM}| \gtrsim 5 \times 10^5$ rad m^{-2} for three out of four epochs). Accordingly, we consider the large RM obtained for 3C 84 within the 43 GHz band to be intrinsic to the source. We also note a discrepancy in the form of a negative RM (i.e., decreasing EVPA value with increasing λ^2), which is present only in Apr 2015. We note that the EVPAs of the calibrators in this epoch generally increase with increasing λ^2 (see the top panel of Fig. 9). If the systematic EVPA rotation in the calibrators were purely due to residual calibration errors, the intrinsic RM of 3C 84 in this epoch would become even more negative.

4. Discussion

4.1. Polarization structure

Here we briefly discuss the possible implications of the polarization structure in the core region. At 86 GHz, the two subnuclear polarization features, P1 and P2, have different degrees of linear polarization. In order to highlight the polarization asymmetry, we chose the 86 GHz image shown in Fig. 7 and made a transverse cut to the core region (in the E–W direction at ∼0.1 mas downstream of the jet). From this slice, we obtained transverse total and polarization intensity profiles (Fig. 12).

A transverse polarization asymmetry in the core region has occasionally been seen in several other AGNs (Gómez et al. 2008, 2016; O'Sullivan & Gabuzda 2009; Clausen-Brown et al. 2011). This is often related to the geometry of the jet (e.g., jet inclination and opening angle) and the magnetic field (e.g., pitch angle; see Lyutikov et al. 2005; Clausen-Brown et al. 2011; Porth et al. 2011). We note that the intrinsic and spatially integrated EVPA is $\chi_{\rm int} \sim -38$ deg in May 2015. This angle is neither parallel nor perpendicular to the position angle of the inner jet (∼170 deg inferred from Fig. 7), suggesting that the orientation of the magnetic field might be oblique to the jet.

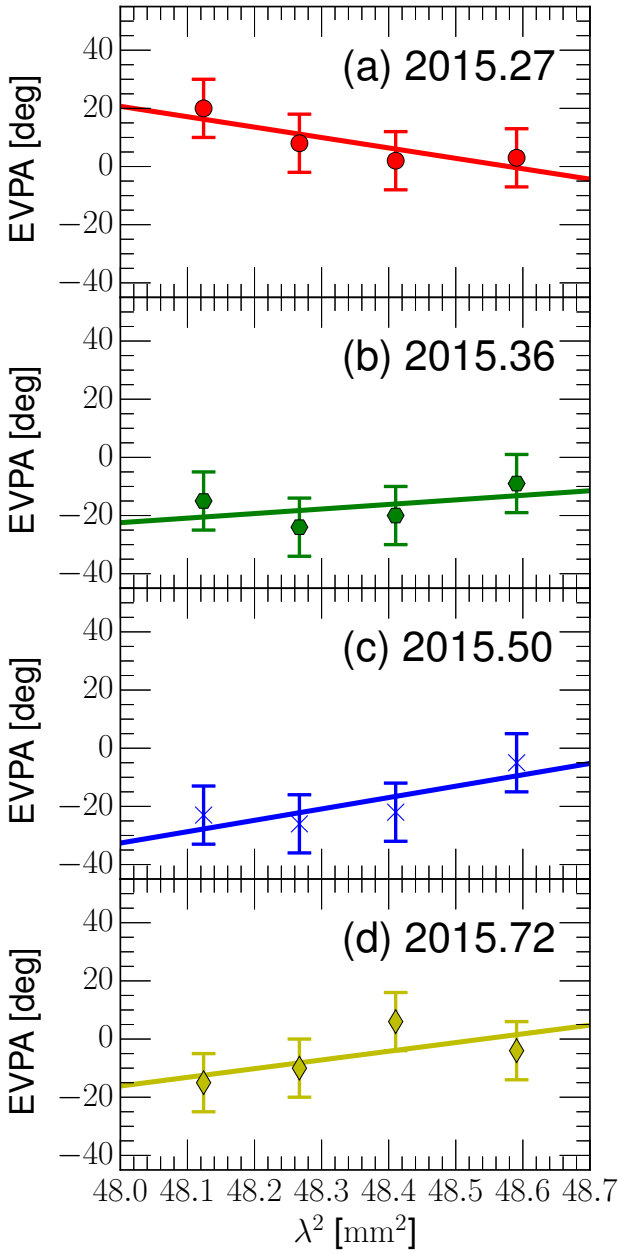

Fig. 10. EVPA of 3C 84 vs. the squared wavelength λ^2 within the VLBA 43 GHz band (error bars) and the best-fit Faraday rotation model (solid line).

However, we also note that the polarization structure is also highly time-variable at 43 GHz during 2015 when the VLBI core flux density showed a small outburst. Such outbursts often accompany structural changes within the jet – for example ejection of new VLBI components from the core – and also likely lead to changes in the polarized morphology near the core. In fact, the peak of the linear polarization in the VLBA 43 GHz images moves with respect to the peak of the total intensity by ∼0.2 mas on an approximately monthly timescale, especially in the E–W direction (see Appendix C). We note that the typical VLBA beam at 43 GHz beam is ∼0.15 mas in E–W direction. Thus the position offset of ∼0.2 mas is larger than the beam size and should be significant. Single-dish monitoring observations of 3C 84 at millimeter wavelengths by Agudo et al. (2018b) also show polarization time-variability on longer timescales. Therefore, one cannot rule out the possibility of turbulence

Table 6. RM within the VLBA 43 GHz band.

Epoch [yyyy/mm/dd]	RM [$\times 10^5$ rad m^{-2}]	χ [deg]
2015/04/12	$-(6.2 \pm 2.6)$	11 ± 5
2015/05/11	2.7 ± 3.5	$-(14 \pm 5)$
2015/07/02	6.8 ± 3.3	$-(11 \pm 5)$
2015/09/22	5.2 ± 4.2	$-(8 \pm 5)$

Notes. From left to right, columns denote the observing epoch, the RM and the EVPA interpolated to the central frequency of the 43 GHz band (43.1155 GHz).

(e.g., Marscher 2014) or varying opacity across the jet which may also produce similar asymmetric and variable polarization structures.

4.2. Possible explanations for the polarization spectrum and EVPA rotation

In the rest of this discussion, we focus on possible physical explanations for the observed frequency dependence of the fractional linear polarization and EVPA. Frequency dependence of the polarization properties can be explained by several scenarios. For instance, the inverted total intensity spectrum (Fig. 5, left) between 15 and 86 GHz suggests high opacity and large synchrotron self-absorption. In such jets, the emission at a higher frequency originates from a region closer to the base of the jet (e.g., Lobanov 1998). If entanglement of the magnetic field were the main source for the low linear polarization at low frequencies, a larger polarization degree $m_{\rm L}$ at higher frequencies could be interpreted as progressively more ordered magnetic fields in the inner jet region (e.g., Agudo et al. 2014, 2018b). Alternatively, the large synchrotron opacity in the core itself can transform the observed polarization, causing the linear polarization to increase with decreasing opacity (i.e., toward shorter wavelengths; see Pacholczyk 1970; Jones & Odell 1977). In particular, the transition from optically thick to optically thin is accompanied by a ~90 deg flip of the EVPA (Pacholczyk 1970).

We point out, however, that the impact of Faraday rotation is also significant because Faraday depolarization is a sensitive function of the observing frequency (Burn 1966; Sokoloff et al. 1998). Certainly, Faraday rotation may be not be a unique explanation of the large EVPA rotations across the observing frequencies. However, we also find large EVPA rotation and the corresponding RM within the 43 GHz band (Fig. 10). This suggests that opacity effects alone cannot explain the results because the opacity change within the 43 GHz band is most likely small given the small fractional bandwidth of 256 MHz/43 GHz $\sim 6 \times 10^{-3}$.

Within this perspective, the spectrum of the circular polarization in 3C 84 is also noteworthy. The inner jet of 3C 84 has a large degree of circular polarization $m_{\rm C} \sim 1$–3% at 15–22 GHz (Homan & Wardle 2004). At higher frequencies, there are still no direct VLBI measurements of the circular polarization in this source. However, single-dish observations suggest that the fractional circular polarization has a flat spectrum between centimeter and millimeter wavelengths ($m_{\rm C} \sim$ a few $\times 0.1\%$ at both 5–8 GHz and 86–230 GHz; Aller et al. 2003; Myserlis et al. 2018; Agudo et al. 2010; Thum et al. 2018). As these authors suggest, the combination of low fractional linear polarization and high circular polarization is presumably produced by Faraday conversion, which is accompanied by Faraday rotation in inhomogeneous plasma that is located within (or perhaps external to) the jet (Jones & Odell 1977; Wardle & Homan 2003; MacDonald & Marscher 2018). Therefore, we investigate in the following the impact of Faraday rotation in terms of Faraday depolarization for different types of Faraday screens.

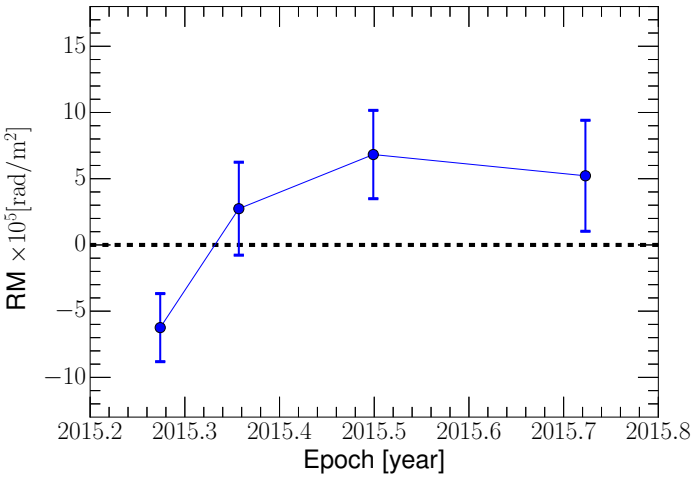

Fig. 11. Time variation of the 43 GHz sub-band RM for 3C 84.

4.3. Faraday depolarization

Based on the previous discussion (Sect. 4.2), we now discuss the impact of the Faraday effect assuming different types of Faraday screens. For the central VLBI core region of 3C 84, an external Faraday screen can be located at various places. For example, a free–free absorption disk (Walker et al. 2000), which might be clumpy (Fujita & Nagai 2017), could act as a Faraday screen. Another possibility is the accretion flow, which surrounds the central engine (Plambeck et al. 2014). We note that a radiatively inefficient accretion flow (RIAF) has been used to interpret the frequency dependence of the linear and circular polarization of Sgr A* (e.g., Bower et al. 2002; Muñoz et al. 2012), which resembles our observations of 3C 84. Finally, the host galaxy of 3C 84 (NGC 1275) contains a substantial amount of intergalactic gas, whose effect is seen on the parsec-scale jet polarization at $\lesssim$22 GHz (Taylor et al. 2006).

In the following we model the Faraday depolarization for three very simple cases. We then discuss their physical implications in subsequent Sects. 4.3.1 and 4.3.2. We assume three types of Faraday screens:

1. A foreground screen with a disordered magnetic field and random RM fluctuations;
2. A foreground screen with an ordered magnetic field and a smooth RM gradient within the observing beam; and
3. A Faraday depolarization inside the jet and a uniform magnetic field.

Following Burn (1966), the observed degree of linear polarization $m_{\rm obs}$ is a function of the observing wavelength, which for the three above cases can be written as:

$$\text{Case I}: \quad m_{\rm obs} = m_0 \exp(-2\sigma^2\lambda^4), \tag{9}$$

$$\text{Case II}: \quad m_{\rm obs} = m_0 \left| \frac{\sin(\Delta {\rm RM}\lambda^2)}{\Delta {\rm RM}\lambda^2} \right|, \tag{10}$$

$$\text{Case III}: \quad m_{\rm obs} = m_0 \left| \frac{\sin(2{\rm RM}\lambda^2)}{2{\rm RM}\lambda^2} \right|, \tag{11}$$

where m_0 is the intrinsic linear polarization degree, λ is the observing wavelength, σ is the standard deviation of the

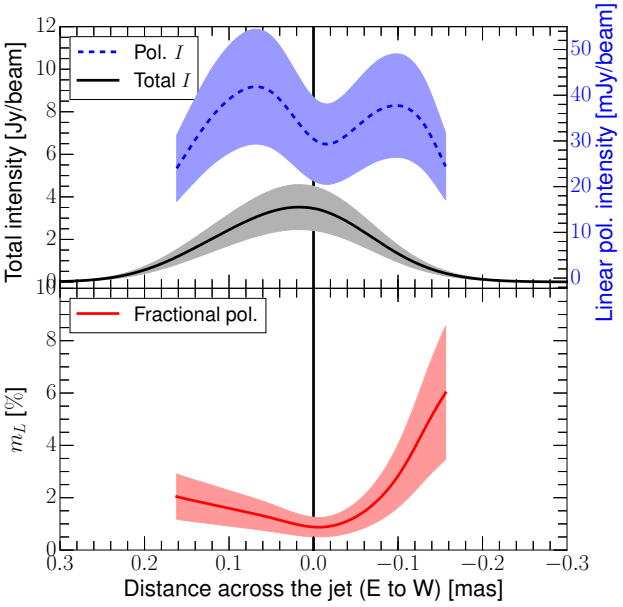

Fig. 12. *Top panel*: total intensity, linear polarization intensity; *bottom panel*: degree of linear polarization at 86 GHz obtained by the slice transverse to the core and calculated by the pixel values in the image plane (negative core separation toward west; see Fig. 7). The solid black line indicates the position of the total intensity peak. The shaded area marks the measurement errors, assuming 30% uncertainty in the flux density measurements at 86 GHz (see Table 4). Only linear polarization higher than 24 mJy beam^{-1} is shown.

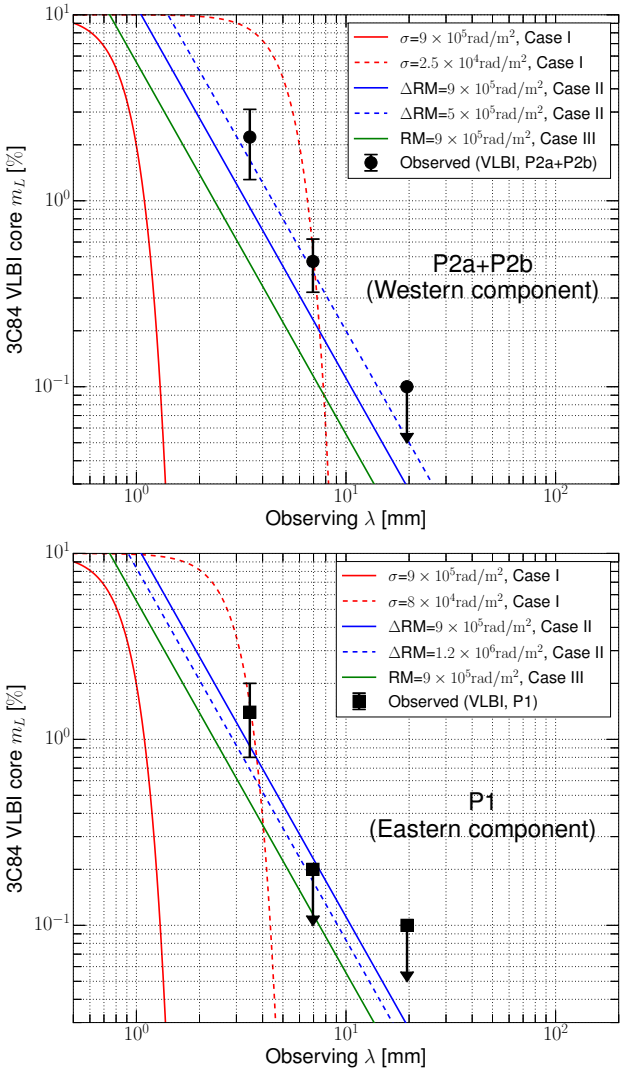

Fig. 13. Upper limits for m_L for external (Case I and II) and internal (Case III) Faraday depolarization and the VLBI polarization from observations. Arrows indicate the upper limits from observations. The *top* and *bottom panels* are for the P2 and P1 components, respectively. See the text for details.

dispersion of the RM in the external Faraday screen, ΔRM is the RM gradient within the beam and RM is the observed rotation measure. For Case I, we assume $\sigma \approx \epsilon \times$ RM where ϵ is a scaling factor describing the level of the RM dispersion (i.e., larger ϵ for more inhomogeneity). We start the calculation with $\epsilon = 1$. Similarly, we assume ΔRM ∼ RM for Case II. For Cases II and III, we have conservative upper limits for $m_{\rm obs}$ by $m_{\rm obs} \leq m_0/(\Delta {\rm RM}\lambda^2)$ and $m_{\rm obs} \leq m_0/(2{\rm RM}\lambda^2)$, respectively. We choose $m_0 = 10\%$, which is the theoretical maximum value in the case of high synchrotron opacity (Pacholczyk 1970). Finally, we take a RM ∼ 9×10^5 rad m^{-2} from Plambeck et al. (2014), which is also close to the largest RM value found in our work (∼7×10^5rad m^{-2}). We then compare the upper limits with the observed $m_{\rm L}$ values in May 2015. For the P2 component, we use the $m_{\rm L}$ values at 86 and 43 GHz of Table 5 and adopt $m_{\rm L} \lesssim 0.1\%$ as an upper limit at 15 GHz. For the P1 component, we take the measured $m_{\rm L}$ value at 86 GHz and adopt $m_{\rm L} \lesssim 0.2\%$ and $\lesssim$0.1% as upper limits for 43 and 15 GHz, respectively. For both components, we use the polarization degrees as measured with the VLBA 43 GHz restoring beam.

In Fig. 13 we show the upper limits for the linear polarization degree calculated for the three depolarization models. The plots reveal several important points. In Case I (red lines), the RM dispersion σ is as large as 9×10^5 rad m^{-2} for $\epsilon \sim 1$. This is apparently problematic for both P2 and P1 because of the strong depolarization (solid red lines). We find that $\sigma \sim 2.5 \times 10^4$ rad m^{-2} is required for P2 in order to explain the observed linear polarization at 43 GHz (dashed red line). An even smaller σ would be required if the intrinsic degree of polarization m_0 were smaller than 10% for a more disordered magnetic field. A σ which is two orders of magnitude smaller than the RM (i.e., $\epsilon \lesssim (2.5\times10^4)/(9\times10^5) \sim 0.03$) indicates a highly uniform RM distribution in the external screen, which requires a well ordered large-scale magnetic field. Similar results are obtained for P1 (σ is at most ∼8×10^4 rad m^{-2} and $\epsilon \lesssim (8\times10^4)/(9\times10^5) \sim 0.09$). In contrast, Case II (blue lines) seems to explain the observed linear polarization in the core much better. We find that for P2 and P1 rotation measure gradients of ΔRM ∼ 5×10^5 rad m^2 and ΔRM ∼ 1.2×10^6 rad m^2 could explain the polarization at ≥43 GHz, respectively (dashed blue lines).

In Case III (green solid lines), the depolarization exceeds the values that we infer from our data and therefore we regard Case III as less likely and do not discuss it further.

Therefore, a smooth RM distribution in the external screen appears to be the most plausible scenario. We now proceed to explore the implications of the model cases I and II and try to distinguish between them.

4.3.1. Case I : Accretion flow as the foreground screen

In the vicinity of the central black hole and depending on its covering factor, a radiatively inefficient accretion flow (RIAF; e.g., Yuan & Narayan 2014) could be regarded as a good candidate for a Faraday screen. In such a flow, magneto-rotational instabilities and magnetohydrodynamic (MHD)

turbulence can introduce a certain degree of inhomogenity in the matter and magnetic field distribution (Balbus & Hawley 1991, 1998). Recently, Johnson et al. (2015) measured the linear polarization in Sgr A* with VLBI at 230 GHz and suggested a short coherence length of the magnetic field orientation, of the order of $\sim 6R_s$. The linear polarization appears more random over larger scales. Adopting this also for the accretion flow of 3C 84 leads to the expectation that the Faraday depth across the screen is comparable to the characteristic Faraday depth (i.e., σ or ΔRM $\sim$ RM). However, this is in contrast to our finding (see Fig. 13). Certainly, our modeling simplifies a number of details in the disk-jet system. However, detailed general relativistic MHD simulations of such an accretion flow also suggest very strong depolarization of the jet by the accretion flow (e.g., Mościbrodzka et al. 2017). Hence, the accretion flow appears to us as a less preferred candidate for the Faraday screen.

Another problem in the association of the large RM in 3C 84 with the accretion flow was pointed out by Plambeck et al. (2014). The authors modeled a spherical accretion flow in 3C 84 using a highly ordered, radial magnetic field, in order to relate the observed RM $\sim 9\times10^5$ rad m^{-2} with the expected mass accretion rate. For realistic estimates of the magnetic field strength and the electron density in the accretion flow, the authors derive a higher RM, so that the observed RM appears to be too small. Therefore, the authors concluded that either (i) the magnetic field strength is much weaker than the equipartition value, (ii) the magnetic field is highly disordered, or (iii) the accretion flow is rather disk-like and the line of sight does not pass through the accretion flow. Indeed, an oblate disk-like geometry of the accretion flow would provide a suitable explanation because it explains the observational findings without fine-tuning the intrinsic physical properties of the accretion flow.

If the observed linear polarization is marginally affected by the disk-like accretion flow because of the geometry, the disk height H to disk radius R ratio H/R should be $\tan^{-1}(H/R) \lesssim (90^\circ - \theta)$ or $H/R \lesssim \tan(90^\circ - \theta)$ where θ is the jet viewing angle. If we adopt $\theta \sim 30^\circ$ ($\sim$60°) from previous observations (Walker et al. 1994; Fujita & Nagai 2017), we find $H/R \lesssim 1.7$ ($\lesssim$0.6). If the thick accretion flow is threaded by a strong poloidal magnetic field which can compress the disk vertically (e.g., McKinney et al. 2012), an even smaller H/R ratio may be physically possible.

4.3.2. Case II : Faraday rotation and depolarization due to the transverse jet stratification

Alternatively, a mildly relativistic sheath surrounding the relativistic jet may provide the required external screen. A wide and collimated jet can be formed by the inner accretion disk or directly by a spinning central black hole (Blandford & Payne 1982; Blandford & Znajek 1977). The rotation of the central engine leads to the development of a stratified and twisted magnetic field topology (e.g., Tchekhovskoy et al. 2015). The boundary layer (or sheath) of such jets may provide the uniform external Faraday screen in Case II. Evidence for an ordered magnetic field configuration in jets comes from a plethora of polarization VLBI jet observations and from observations of transverse RM gradients on parsec scales (e.g., Zavala & Taylor 2005; Hovatta et al. 2012; Gabuzda et al. 2017). The magnetic field is expected to be more ordered in the inner jet region when the jet-launching region becomes magnetically dominated (e.g., Zamaninasab et al. 2014; Martí-Vidal et al. 2015).

High-angular-resolution VLBI observations of the inner jet of 3C 84 show a limb-brightened morphology (see Fig. 7 and also Giovannini et al. 2018). A limb-brightened jet most likely consists of at least two different jet components with different speeds, electron densities, or magnetic field strengths (spine-sheath geometry; e.g., Pelletier & Roland 1989; Komissarov 1990). Mildly relativistic electrons in the boundary layer of the jet, possibly mixed with thermal particles, will then cause Faraday rotation and conversion (Sokoloff et al. 1998; Perlman et al. 1999; Pushkarev et al. 2005; Porth et al. 2011; MacDonald et al. 2015; Pasetto et al. 2016; Lico et al. 2017). In Fig. 14 we show a sketch of a stratified jet for illustration.

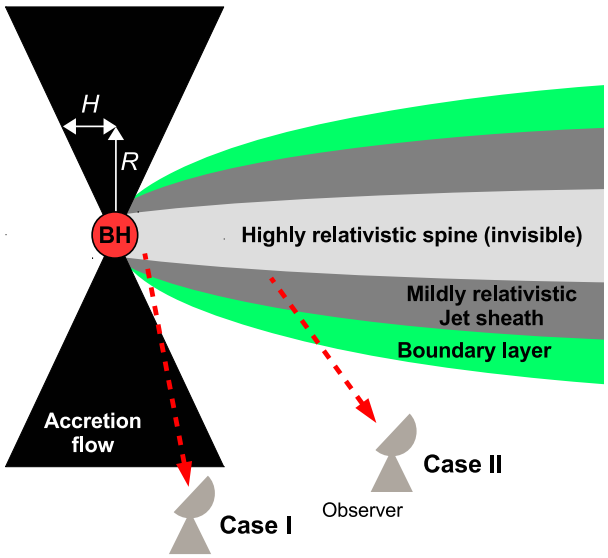

Fig. 14. Illustration of the geometry discussed throughout Sects. 4.3.1 and 4.3.2. We note that the figure is not drawn to scale.

4.4. Estimation of the jet magnetic field strength and the electron density

In the following we assume that the boundary layer of the jet is the Faraday screen and is responsible for the observed RM. We estimate the jet electron number density adopting the jet magnetic field strength from the synchrotron self-absorption theory. In convenient units, the observed RM can be written as follows:

$$\frac{\mathrm{RM}}{\mathrm{rad\,m^{-2}}} = 8.1\times10^5 \int_{\mathrm{source}}^{\mathrm{telescope}} \left(\frac{n_\mathrm{e}}{\mathrm{cm^{-3}}}\right)\left(\frac{B_\parallel}{G}\right)\left(\frac{\mathrm{d}l}{\mathrm{pc}}\right), \quad (12)$$

where n_e is the number density of the thermal electrons between the source and the telescope, $B_\parallel$ is the line-of-sight component of the magnetic field and dl is the path length through the plasma from the source toward the observer.

We calculate the synchrotron self-absorption (SSA) magnetic field strength B_SSA in the core following Marscher (1983);

$$B_\mathrm{SSA} = 10^{-5} b(\alpha) \frac{\theta_\mathrm{m}^4 \nu_\mathrm{m}^5 \delta}{S_\mathrm{m}^2 (1+z)} \mathrm{Gauss}, \quad (13)$$

where $b(\alpha)$ is a constant tabulated in Marscher (1983) as a function of the spectral index, S_m is the flux density (in Jy) at the turnover frequency ν_m (in GHz), θ_m is the source angular size (in mas) at ν_m and δ is the Doppler factor. We note that the exact value of ν_m is not accurately determined by our data (see the spectrum in Fig. 5). However, this spectrum and recent VLBI observations of 3C 84 at 86 GHz and 129 GHz

(Hodgson et al. 2018) suggest a spectral turnover near 86 GHz. Therefore, we adopt $\nu_m = 86$ GHz for the calculation of B_{SSA}. For the optically thin spectrum we use $\alpha = -0.5$, which fixes $b(\alpha) = 3.2$. Assuming $\nu_m = 86$ GHz, $S_m = (5.6 \pm 1.7)$ Jy and $\theta_m = 1.8 \times (0.14 \pm 0.01)$ mas[7], we obtain $B_{SSA} \sim (19 \pm 13) \times \delta$ G.

For the jet viewing angle $\theta \sim 30°-60°$ and the apparent jet speed $\sim 0.1c$ near the core, the Doppler factor is $\delta \sim 1.1$. With this, we obtain $B_{SSA} \sim (21 \pm 14)$ G. We note that Abdo et al. (2009) and Aleksić et al. (2014) suggest a relatively large Doppler factor of $\delta \sim 2-4$ based on the theoretical modeling of the synchrotron self-Compton process in the jet. In this case, the resulting magnetic field strength would be $\sim(2-4)$ times larger.

We take B_{SSA} as the average magnetic field strength in the jet and calculate the average electron number density n_e by

$$\frac{n_e}{\mathrm{cm}^{-3}} \sim 1.2 \times 10^{-6} \left(\frac{\mathrm{RM}}{\mathrm{rad\,m}^{-2}}\right) \left(\frac{B_{SSA}}{G}\right)^{-1} \left(\frac{\theta_m}{\mathrm{pc}}\right)^{-1}, \quad (14)$$

where we assume that the size θ_m, is a lower limit to the approximate path length for the jet medium because a longer path length is expected for a deprojected line-of-sight. For RM $= 9 \times 10^5$ rad m^{-2}, we obtain $n_e \leq (0.6 \pm 0.4)$ cm^{-3}. The density will be even lower if the Doppler factor is larger and the magnetic field strength is higher. In any case, the density is an order of magnitude lower than an ambient gas density estimate of $n_e \sim 8$ cm^{-3} obtained by Fujita & Nagai (2017) for the central parsecs. A low jet density is not implausible and is consistent with jet collimation by a denser ambient medium (e.g., Nagai et al. 2014; Giovannini et al. 2018).

We note that our calculations make simplified assumptions with regards to the magnetic field strength, the path length and the jet geometry. Future more detailed calculations using numerical radiative transfer across all Stokes parameters (e.g., MacDonald & Marscher 2018) should be able to constrain these parameters more precisely. Also, the exact value of the turnover frequency on this spatial scale is still relatively uncertain. Quasi-simultaneous global mm-VLBI observations with the GMVA and the Event Horizon Telescope (e.g., Doeleman et al. 2012; Lu et al. 2018) will help to determine the spectral properties of the innermost jet and central engine.

5. Summary and conclusions

In this paper, we presented a study of the polarization properties of the radio galaxy 3C 84 based on the results from polarimetric VLBI observations of the source at mm-wavelengths. We summarize our findings and main conclusions as follows:

1. We found asymmetrically distributed and polarized emission in the VLBI core region of 3C 84 at 86 GHz using GMVA observations. The east-west oriented and linearly polarized structure consists of two polarized components (P1 and P2), which are separated by $\sim$0.2 mas (corresponding to $\sim$0.07 pc $\sim 812 R_s$). The fractional linear polarization m_L of P1 and P2 at 86 GHz is $\sim$2% with the VLBA 43 GHz beam.
2. Additional close-in-time VLBA 43 GHz polarization images also reveal the presence of polarized emission ($m_L \sim 0.4-0.5\%$). The polarized structure is also time-variable. The moving direction of the variable polarized emission feature, which is almost perpendicular to the milliarcsecond jet, suggests that the jet base may be edge-brightened in polarized light. However, other effects such as ejection of a new VLBI component or opacity effects across the jet cannot be excluded.
3. The total intensity spectrum of 3C 84 is inverted up to at least 86 GHz and the linear polarization m_L increases with frequency following a power-law $m_L \propto \nu^{0.77}$. A likely explanation invokes a decreasing synchrotron opacity and lower Faraday depolarization at higher frequencies.
4. The combination of quasi-simultaneous EVPA measurements at 43 and 86 GHz and adding near in time EVPA measurements from ALMA at higher frequencies, reveals a high rotation measure in the VLBI core region of RM $\sim 2 \times 10^5$ rad m^{-2} at $\gtrsim$43 GHz in May 2015. This is comparable to the RM measurements at 230 GHz on larger angular scales (Plambeck et al. 2014).
5. A significant rotation of the EVPA is also observed within the 43 GHz VLBA observing band and also suggests the presence of Faraday rotation. Repeated measurements of the RM within the 43 GHz VLBA observing band are consistent with the high RM in the VLBI core region at three epochs, but also suggest that the RM has changed its sign at one epoch. This could be related to the onset of a small total intensity flare in the VLBI core in 2015.
6. In order to explain the degree of linear polarization by Faraday depolarization, an external screen with either a small RM dispersion or only a smoothly varying uniform RM distribution is required.
7. The data would support a tentative association of the Faraday screen with the accretion flow if (i) the accretion flow was found to be thick ($H/R \geq 1.7$ for the jet viewing angle $\theta = 30°$) and more importantly (ii) the magnetic field was highly ordered. However, the latter appears to be in contradiction with the results of previous studies (e.g., Plambeck et al. 2014). Instead, a stratified jet with a boundary layer containing an ordered magnetic field configuration could also provide a good explanation for the large RM, the frequency dependence of the depolarization and possibly also for the RM variability. The edge-brightened jet morphology observed at 22 GHz (Giovannini et al. 2018) would also support this interpretation.
8. From synchrotron self-absorption theory, we calculate a magnetic field strength in the VLBI core region of 3C 84 of $B_{SSA} = (21 \pm 14)$ G, adopting an only mild relativistic beaming with a Doppler factor of $\delta \sim 1.1$ from jet kinematics. In this case a jet electron density of $n_e \leq (0.6 \pm 0.4)$ cm^{-3} is required to explain the observed high RM. The field strength would be larger by factor $\sim$2–4 if a higher Doppler factor of $\delta \sim 2-4$ is used and the electron density will be correspondingly lower. In both cases the jet electron density appears to be at least an order of magnitude lower than the density of the ambient gas.

Overall, our study suggests that either the accretion flow or a transversely stratified jet with boundary layers can play an important role in the generation of the polarized mm-wave emission in the milliparsec scale VLBI structure. Future millimeter VLBI imaging, performed quasi-simultaneously at different frequencies and including VLBI observations above 86 GHz, will help to better understand the complicated nature of the polarization in 3C 84. Also, a more detailed theoretical modeling of the linear and circular polarization spectrum and complemented by numerical simulations, would be very beneficial. Finally, we note that the detection of significant linear polarization at the jet base in 3C 84 may shed light on the properties of the Faraday screen in other radio galaxies (e.g., M 87; Kim et al. 2018). Further studies should prove fruitful.

[7] The factor 1.8 corrects for the geometry (Marscher 1983).

Acknowledgements. We thank the anonymous referee for valuable comments and suggestions, which greatly helped to improve the paper. We thank Carolina Casadio and Ioannis Myserlis for fruitful discussions and comments. J.-Y.K. is supported for this research by the International Max-Planck Research School (IMPRS) for Astronomy and Astrophysics at the University of Bonn and Cologne. I.A. acknowledges support by a Ramón y Cajal grant of the Ministerio de Economía, Industria y Competitividad (MINECO) of Spain and by and additional MINECO grant with reference AYA2016–80889–P. R.-S. L. is supported by the National Youth Thousand Talents Program of China and by the Max-Planck Partner Group. This research has made use of data obtained with the Global Millimeter VLBI Array (GMVA), which consists of telescopes operated by the MPIfR, IRAM, Onsala, Metsahovi, Yebes, the Korean VLBI Network, the Green Bank Observatory and the Long Baseline Observatory. The VLBA is an instrument of the Long Baseline Observatory, which is a facility of the National Science Foundation operated by Associated Universities, Inc. The data were correlated at the correlator of the MPIfR in Bonn, Germany. This work made use of the Swinburne University of Technology software correlator, developed as part of the Australian Major National Research Facilities Programme and operated under licence. This study makes use of 43 GHz VLBA data from the VLBA-BU Blazar Monitoring Program (VLBA-BU-BLAZAR; http://www.bu.edu/blazars/VLBAproject.html), funded by NASA through the Fermi Guest Investigator Program. This research has made use of data from the MOJAVE database that is maintained by the MOJAVE team (Lister et al. 2009). This paper makes use of the following ALMA data: ADS/JAO.ALMA#2011.0.00001.CAL. ALMA is a partnership of ESO (representing its member states), NSF (USA) and NINS (Japan), together with NRC (Canada), MOST and ASIAA (Taiwan) and KASI (Republic of Korea), in cooperation with the Republic of Chile. The Joint ALMA Observatory is operated by ESO, AUI/NRAO and NAOJ. This research has made use of data from the OVRO 40 m monitoring program (Richards et al. 2011). The OVRO 40 M Telescope Fermi Blazar Monitoring Program is supported by NASA under awards NNX08AW31G and NNX11A043G, and by the NSF under awards AST-0808050 and AST-1109911.

References

Abdo, A. A., Ackermann, M., Ajello, M., et al. 2009, ApJ, 699, 31
Agudo, I., Thum, C., Wiesemeyer, H., & Krichbaum, T. P. 2010, ApJS, 189, 1
Agudo, I., Marscher, A. P., Jorstad, S. G., et al. 2012, ApJ, 747, 63
Agudo, I., Thum, C., Gómez, J. L., & Wiesemeyer, H. 2014, A&A, 566, A59
Agudo, I., Thum, C., Molina, S. N., et al. 2018a, MNRAS, 474, 1427
Agudo, I., Thum, C., Ramakrishnan, V., et al. 2018b, MNRAS, 473, 1850
Aleksić, J., Ansoldi, S., Antonelli, L. A., et al. 2014, A&A, 564, A5
Aller, H. D., Aller, M. F., & Plotkin, R. M. 2003, Ap&SS, 288, 17
Balbus, S. A., & Hawley, J. F. 1991, ApJ, 376, 214
Balbus, S. A., & Hawley, J. F. 1998, Rev. Mod. Phys., 70, 1
Blandford, R. D., & Payne, D. G. 1982, MNRAS, 199, 883
Blandford, R. D., & Znajek, R. L. 1977, MNRAS, 179, 433
Boccardi, B., Krichbaum, T. P., Ros, E., & Zensus, J. A. 2017, A&ARv, 25, 4
Bower, G. C., Falcke, H., Sault, R. J., & Backer, D. C. 2002, ApJ, 571, 843
Burn, B. J. 1966, MNRAS, 133, 67
Casadio, C., Gómez, J. L., Jorstad, S. G., et al. 2015, ApJ, 813, 51
Casadio, C., Krichbaum, T., Marscher, A., et al. 2017, Galaxies, 5, 67
Clausen-Brown, E., Lyutikov, M., & Kharb, P. 2011, MNRAS, 415, 2081
Deller, A. T., Brisken, W. F., Phillips, C. J., et al. 2011, Publ. Astron. Soc. Pac., 123, 275
Doeleman, S. S., Fish, V. L., Schenck, D. E., et al. 2012, Science, 338, 355
Fujita, Y., & Nagai, H. 2017, MNRAS, 465, L94
Gabuzda, D. C., Roche, N., Kirwan, A., et al. 2017, MNRAS, 472, 1792
Giovannini, G., Savolainen, T., Orienti, M., et al. 2018, Nat. Astron., 33
Gómez, J. L., Marscher, A. P., Jorstad, S. G., Agudo, I., & Roca-Sogorb, M. 2008, ApJ, 681, L69
Gómez, J. L., Lobanov, A. P., Bruni, G., et al. 2016, ApJ, 817, 96
Greisen, E. W. 1990, in Acquisition, Processing and Archiving of Astronomical, eds. G. Longo, & G. Sedmak, 125
Hodgson, J. A., Krichbaum, T. P., Marscher, A. P., et al. 2017, A&A, 597, A80
Hodgson, J. A., Rani, B., Lee, S.-S., et al. 2018, MNRAS, 475, 368
Homan, D. C., & Wardle, J. F. C. 2004, ApJ, 602, L13
Hovatta, T., Lister, M. L., Aller, M. F., et al. 2012, AJ, 144, 105
Jackson, N., Browne, I. W. A., Battye, R. A., Gabuzda, D., & Taylor, A. C. 2010, MNRAS, 401, 1388
Johnson, M. D., Fish, V. L., Doeleman, S. S., et al. 2015, Science, 350, 1242
Jones, T. W., & Odell, S. L. 1977, ApJ, 214, 522
Jorstad, S. G., Marscher, A. P., Lister, M. L., et al. 2005, AJ, 130, 1418
Jorstad, S. G., Marscher, A. P., Stevens, J. A., et al. 2007, AJ, 134, 799
Jorstad, S. G., Marscher, A. P., Morozova, D. A., et al. 2017, ApJ, 846, 98
Kim, J. Y., Krichbaum, T. P., Lu, R. S., et al. 2018, A&A, 616, A188
Komissarov, S. S. 1990, Sov. Astron. Lett., 16, 284
Koyama, S., Kino, M., Giroletti, M., et al. 2016, A&A, 586, A113
Leppanen, K. J., Zensus, J. A., & Diamond, P. J. 1995, AJ, 110, 2479
Lico, R., Gómez, J. L., Asada, K., & Fuentes, A. 2017, MNRAS, 469, 1612
Lister, M. L., & Homan, D. C. 2005, AJ, 130, 1389
Lister, M. L., Aller, H. D., Aller, M. F., et al. 2009, AJ, 137, 3718
Lobanov, A. P. 1998, A&A, 330, 79
Lu, R.-S., Krichbaum, T. P., Roy, A. L., et al. 2018, ApJ, 859, 60
Lyutikov, M., Pariev, V. I., & Gabuzda, D. C. 2005, MNRAS, 360, 869
MacDonald, N. R., & Marscher, A. P. 2018, ApJ, 862, 58
MacDonald, N. R., Marscher, A. P., Jorstad, S. G., & Joshi, M. 2015, ApJ, 804, 111
Marscher, A. P. 1983, ApJ, 264, 296
Marscher, A. P. 2014, ApJ, 780, 87
Martí-Vidal, I., Krichbaum, T. P., Marscher, A., et al. 2012, A&A, 542, A107
Martí-Vidal, I., Muller, S., Vlemmings, W., Horellou, C., & Aalto, S. 2015, Science, 348, 311
McKinney, J. C., Tchekhovskoy, A., & Blandford, R. D. 2012, MNRAS, 423, 3083
Montier, L., Plaszczynski, S., Levrier, F., et al. 2015a, A&A, 574, A135
Montier, L., Plaszczynski, S., Levrier, F., et al. 2015b, A&A, 574, A136
Mościbrodzka, M., Dexter, J., Davelaar, J., & Falcke, H. 2017, MNRAS, 468, 2214
Muñoz, D. J., Marrone, D. P., Moran, J. M., & Rao, R. 2012, ApJ, 745, 115
Myserlis, I., Angelakis, E., Kraus, A., et al. 2018, A&A, 609, A68
Nagai, H., Haga, T., Giovannini, G., et al. 2014, ApJ, 785, 53
Nagai, H., Fujita, Y., Nakamura, M., et al. 2017, ApJ, 849, 52
O'Sullivan, S. P., & Gabuzda, D. C. 2009, MNRAS, 393, 429
Pacholczyk, A. G. 1970, Radio Astrophysics. Nonthermal Processes in Galactic and Extragalactic Sources (San Francisco: Freeman)
Pasetto, A., Carrasco-González, C., Bruni, G., et al. 2016, Galaxies, 4, 66
Pelletier, G., & Roland, J. 1989, A&A, 224, 24
Perlman, E. S., Biretta, J. A., Zhou, F., Sparks, W. B., & Macchetto, F. D. 1999, AJ, 117, 2185
Plambeck, R. L., Bower, G. C., Rao, R., et al. 2014, ApJ, 797, 66
Porth, O., Fendt, C., Meliani, Z., & Vaidya, B. 2011, ApJ, 737, 42
Pushkarev, A. B., Gabuzda, D. C., Vetukhnovskaya, Y. N., & Yakimov, V. E. 2005, MNRAS, 356, 859
Rani, B., Krichbaum, T. P., Marscher, A. P., et al. 2015, A&A, 578, A123
Richards, J. L., Max-Moerbeck, W., Pavlidou, V., et al. 2011, ApJS, 194, 29
Roberts, D. H., Wardle, J. F. C., & Brown, L. F. 1994, ApJ, 427, 718
Scharwächter, J., McGregor, P. J., Dopita, M. A., & Beck, T. L. 2013, MNRAS, 429, 2315
Schinzel, F. K., Lobanov, A. P., Taylor, G. B., et al. 2012, A&A, 537, A70
Shepherd, M. C., Pearson, T. J., & Taylor, G. B. 1994, Bull. Am. Astron. Soc., 26, 987
Sokoloff, D. D., Bykov, A. A., Shukurov, A., et al. 1998, MNRAS, 299, 189
Strauss, M. A., Huchra, J. P., Davis, M., et al. 1992, ApJS, 83, 29
Suzuki, K., Nagai, H., Kino, M., et al. 2012, ApJ, 746, 140
Taylor, G. B., Gugliucci, N. E., Fabian, A. C., et al. 2006, MNRAS, 368, 1500
Tchekhovskoy, A. 2015, in The Formation and Disruption of Black Hole Jets, eds. I. Contopoulos, D. Gabuzda, & N. Kylafis, Astrophysics and Space Science Library, 414, 45
Thompson, A. R., Moran, J. M., & Swenson, G. W. 2017, Interferometry and Synthesis in Radio Astronomy, 3rd edn.
Thum, C., Wiesemeyer, H., Paubert, G., Navarro, S., & Morris, D. 2008, PASP, 120, 777
Thum, C., Agudo, I., Molina, S. N., et al. 2018, MNRAS, 473, 2506
Trippe, S., Bremer, M., Krichbaum, T. P., et al. 2012, MNRAS, 425, 1192
Walker, R. C., Romney, J. D., & Benson, J. M. 1994, ApJ, 430, L45
Walker, R. C., Dhawan, V., Romney, J. D., Kellermann, K. I., & Vermeulen, R. C. 2000, ApJ, 530, 233
Wardle, J. F. C., & Homan, D. C. 2003, Ap&SS, 288, 143
Wardle, J. F. C., & Kronberg, P. P. 1974, ApJ, 194, 249
Yuan, F., & Narayan, R. 2014, ARA&A, 52, 529
Zamaninasab, M., Clausen-Brown, E., Savolainen, T., & Tchekhovskoy, A. 2014, Nature, 510, 126
Zavala, R. T., & Taylor, G. B. 2005, ApJ, 626, L73

Appendix A: Flux density calibration of 3C 84 using 86 GHz GMVA data in May 2015

Here we discuss a method to improve the accuracy of the absolute flux density calibration of 3C 84 at 86 GHz based on the available a-priori GMVA amplitude calibration, which is not accurate enough (see also Koyama et al. 2016). We compared the multifrequency VLBI flux densities of 3C 84 (Sects. 2.1 and 2.2) with the total flux densities measured by other instruments. At $\nu = 15$ GHz, the Owens Valley Radio Observatory (OVRO; Richards et al. 2011) monitoring program[8] provided near-in-time flux density measurements of $S = 31.8 \pm 0.5$ Jy and $S = 32.3 \pm 0.1$ Jy for 3C 84 on 03 Apr 2015 and 27 Jun 2015, respectively. We averaged the two fluxes in order to estimate the total flux in May 2015 and took half of their difference as the associated error, finding $S = 32.1 \pm 0.3$ Jy. At $\nu \gtrsim 86$ GHz, we refer to Sect. 2.4 for the ALMA flux density measurements. In Fig. A.1 we show (i) the VLBI-scale flux density of the source within ∼4 mas from the core ($S_{\rm VLBI}$), (ii) the VLBI-scale flux density only for the extended jet (∼2–4 mas from the core; $S_{\rm Jet}$) and (iii) the total (i.e., spatially unresolved) flux density measured by the OVRO and the ALMA observations ($S_{\rm tot}$). The GMVA flux densities were taken from only the self-calibrated data, based on the a-priori calibration. We fitted a power-law model to the total flux density (i.e., $S_{\rm VLBI} \propto \nu^{+\alpha}$) in order to estimate the VLBI flux density $S_{\rm VLBI}$ at 43 and 86 GHz. The total flux density spectrum is fitted by $S_{\rm tot} \propto \nu^{-(0.45\pm0.04)}$. From this we estimate $S_{\rm tot}$ at 43 and 86 GHz and calculated the VLBI-to-total flux density ratio $S_{\rm VLBI}/S_{\rm tot}$ (i.e., the compactness). At 15 and 43 GHz, the flux ratio is comparable (∼0.90 and ∼0.84 at 15 GHz and 43 GHz, respectively). However at 86 GHz, it is much lower ($S_{\rm VLBI}/S_{\rm tot} \sim 0.40$). The comparison of the spectral index of the extended jet emission yields a spectral index of $\alpha_{15-43\,\rm GHz} \sim -0.5$, while the spectral index from 43 to 86 GHz is much steeper; $\alpha_{43-86\,\rm GHz} \sim -1.8$. Such a steep spectrum is unlikely and is inconsistent with ALMA measurements between 98 and 344 GHz. We therefore take this as another indication of overly low flux densities at 86 GHz.

To check for an overall scaling problem of the GMVA amplitude calibration we examined the compactness ratio $S_{\rm VLBI}/S_{\rm tot}$ also for other calibrators at 86 GHz (3C 454.3, BLLac, CTA 102 and OJ 287), for which we find – applying a similar procedure as described above – compactness ratios of typically 0.9 at 15 and 43 GHz, but ∼0.5 at 86 GHz. In the following we assume

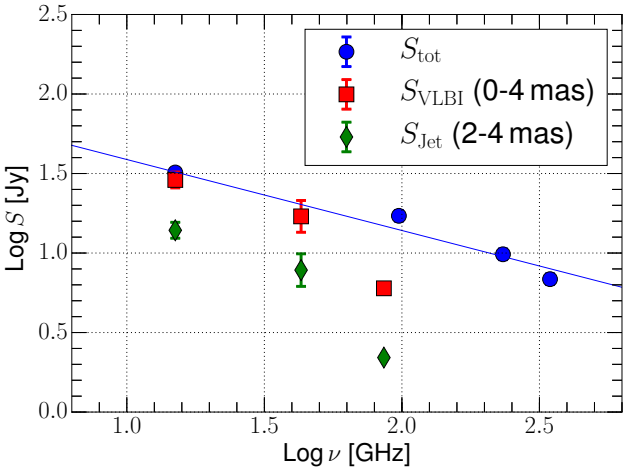

Fig. A.1. Quasi-simultaneous total and VLBI-scale flux densities of 3C 84 in May 2015 displayed in log–log scale. The blue solid line shows the power-law fitted to the total flux measurements. We omit the error bars for the GMVA 86 GHz data points.

that the true compactness $S_{\rm VLBI}/S_{\rm tot}$ at 15, 43 and 86 GHz is comparable. Then the visibility amplitudes of the GMVA data of 3C 84 can be upscaled by a factor $g \sim 2.1$–2.3. Confidence for this number also comes from similar factors obtained for the other calibrators. With this correction factor a much more realistic value of the (optically thin) jet spectral index $\alpha_{43-86\,\rm GHz} \sim -0.8$ is obtained. The corrected total flux density (∼12 Jy) is now also in good agreement with other near-in-time VLBI flux density measurements at 86 GHz reported in literature (e.g., $S \sim (10$–$15)$ Jy; see Hodgson et al. 2018).

In the following we discuss the uncertainty Δg of the scaling value g, which depends on the validity of our assumptions and we could alternatively assume the same spectral index from 15 GHz to 86 GHz for $S_{\rm Jet}$. Assuming a constant spectral index $\alpha_{15-86\,\rm GHz} \sim -0.5$ results in a slightly larger correction factor of $g \sim 2.5$. The range of the $g \sim 2.1$–2.5 suggests that its uncertainty is $\Delta g \sim 0.4$, corresponding to a ∼20% of error in the absolute flux density. It would be overly optimistic to claim an error smaller than ∼20% without having identified the origin of the amplitude scaling error. Therefore, we adopted a slightly larger value of ∼30% for the systematic uncertainty in the measured VLBI flux densities (for this particular epoch).

[8] http://www.astro.caltech.edu/ovroblazars/

Appendix B: Robustness of the polarization imaging at 86 GHz

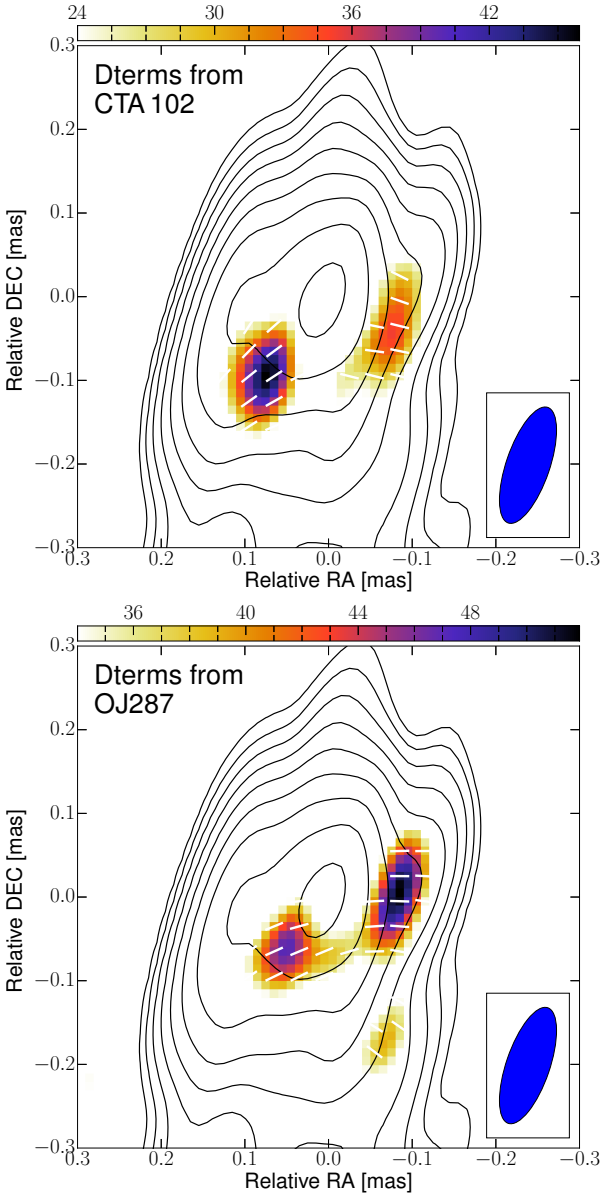

Fig. B.1. Linear polarization maps of the nuclear region of 3C 84 at 86 GHz obtained with different polarization calibrations. The two maps were reconstructed using the D-terms obtained from CTA 102 (*upper panel*) and from OJ 287 (*lower panel*), respectively. The minimum contour level is 7 mJy beam^{-1}.

In order to illustrate the impact of slightly different D-terms on the polarization image of the GMVA data, we made different linear polarization images of 3C 84 using D-terms determined from the individual calibrators. Two examples are shown in Fig. B.1. We find that two central polarization features are reproduced in the nuclear region at similar locations with similar EVPAs. We note that the structure of the jet of OJ 287 is substantially different from that of CTA 102 (e.g., Agudo et al. 2012; Casadio et al. 2015; Hodgson et al. 2017). Despite this, the two polarization maps shown in Fig. B.1 look similar, which provides confidence of the polarization calibration and imaging of 3C 84. Nevertheless, we consider that the polarization image in the main text, which is obtained with the averaged D-terms, is of better quality than those in Fig. B.1 for the reasons explained in the main text.

Appendix C: Multiepoch VLBA 43 GHz data

Table C.1. Properties of the polarized components at 43 GHz obtained from the polarization imaging at four different IFs.

Epoch (1) [yyyy/mm/dd]	$\nu_{\rm obs}$ (2) [GHz]	$S_\nu{}^a$ (3) [Jy]	$m_{\rm L}$ (4) [%]	χ (5) [deg]
2015/04/11	43.0075	1.4 ± 0.1	0.73 ± 0.23	3 ± 10
	43.0875		0.76 ± 0.24	2 ± 10
	43.1515		0.61 ± 0.19	8 ± 10
	43.2155		0.32 ± 0.10	20 ± 10
2015/05/11	43.0075	2.0 ± 0.2	0.44 ± 0.14	−(9 ± 10)
	43.0875		0.49 ± 0.16	−(20 ± 10)
	43.1515		0.53 ± 0.17	−(24 ± 10)
	43.2155		0.43 ± 0.13	−(15 ± 10)
2015/07/02	43.0075	3.6 ± 0.4	0.37 ± 0.12	−(5 ± 10)
	43.0875		0.40 ± 0.13	−(22 ± 10)
	43.1515		0.67 ± 0.21	−(26 ± 10)
	43.2155		0.47 ± 0.15	−(23 ± 10)
2015/09/22	43.0075	2.8 ± 0.3	0.28 ± 0.09	−(4 ± 10)
	43.0875		0.37 ± 0.10	6 ± 10
	43.1515		0.33 ± 0.11	−(10 ± 10)
	43.2155		0.38 ± 0.12	−(15 ± 10)

Notes. The columns show (1) the observing epoch, (2) the observing frequency at each IF, (3) the total flux, (4) the degree of linear polarization, and (5) the EVPA. The total flux was consistent across the frequency in each epoch and we report the measurement only for a single IF. [(a)]The time-variable total flux density of the polarized component is due to not only the flux variability but also the different positions of the peak of the polarization.

Table C.2. The unpolarized core flux (in Jy), the peak (in Jy beam^{-1}) and the core FWHM size (in mas) during 2015 measured from the archival VLBA 43 GHz data sets by the model-fitting analysis.

Epoch [yyyy/mm/dd]	Flux [Jy]	Peak [Jy beam^{-1}]	FWHM size [mas]
2015/02/14	3.9 ± 0.7	3.6 ± 0.5	0.12 ± 0.01
2015/04/11	4.5 ± 0.6	4.1 ± 0.4	0.13 ± 0.01
2015/05/11	4.8 ± 0.7	4.4 ± 0.4	0.13 ± 0.01
2015/06/09	5.8 ± 0.6	5.2 ± 0.4	0.14 ± 0.01
2015/07/02	5.8 ± 0.6	5.2 ± 0.4	0.16 ± 0.01
2015/08/01	5.0 ± 0.5	4.5 ± 0.3	0.16 ± 0.01
2015/09/22	5.0 ± 0.6	4.4 ± 0.4	0.16 ± 0.01
2015/12/05	4.1 ± 0.5	3.7 ± 0.3	0.15 ± 0.01

Notes. A circular beam of 0.3 mas was used for all epochs.

In Table C.1 we show the results of the VLBA 43 GHz polarization measurements in the four different epochs. We provide the polarization maps of the corresponding epochs obtained from the frequency-averaged visibilities in Fig. C.1. The core flux and the FWHM size during 2015 are given in Table C.2.

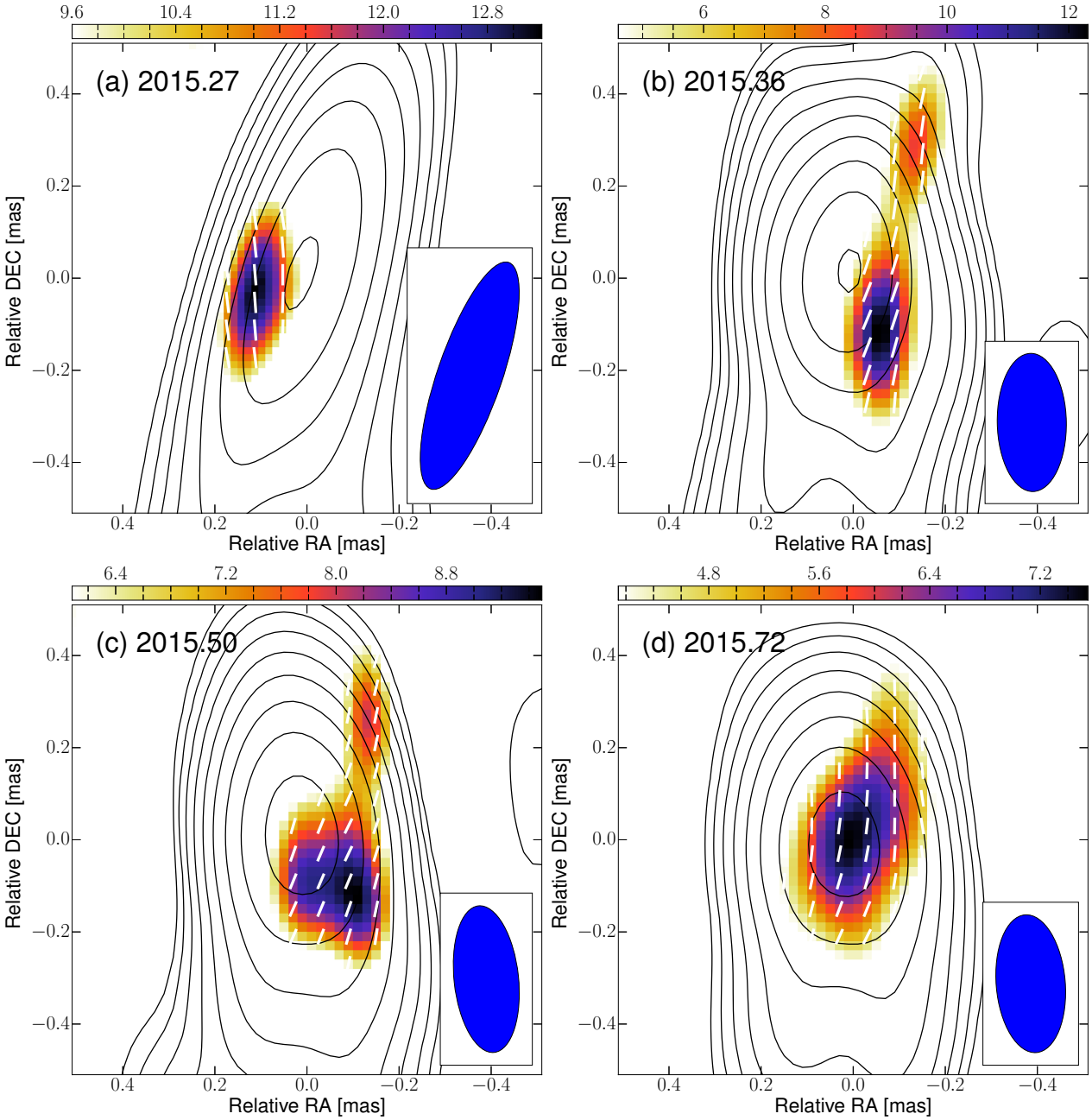

Fig. C.1. VLBA 43 GHz polarization images of 3C 84 zoomed into the core. Labels in the upper left of each panel denotes the observing epoch. The contours show the total intensity and start from 25, 7, 10 and 20 mJy beam^{-1} and increase by factor of two for the *panels a, b, c and d*, respectively. The color bar indicates the linear polarization intensity in mJy beam^{-1}.